The Response of the ECMWF Model to Changes in the Cloud Overlap Assumption

JEAN-JACQUES MORCRETTE AND CHRISTIAN JAKOB

European Centre for Medium-Range Weather Forecasts, Reading, United Kingdom

ABSTRACT

The role of the cloud overlap assumption (COA) in organizing the cloud distribution through its impact on the vertical heating/cooling rate profile by radiative and precipitative/evaporative processes is studied in a series of experiments with a recent version of the ECMWF general circulation model, which includes a prognostic cloud scheme.

First, the radiative forcing initially obtained for different COAs (maximum, MAX; maximum-random, MRN; and random, RAN overlap) is discussed from results of one-dimensional radiation-only computations. Ensembles of $T_L 95$ L31 simulations for the winter 1987/88 (November–December–January–February) are then used, with the three different overlap assumptions applied on radiation only (RAD), evaporation/precipitation only (EP), or both (EPR). In RAD and EPR simulations, the main effect of a change in COA is felt by the model through the change in radiative heating profile, which affects in turn most aspects of the energy and hydrological budget. However, the role of the COA on the precipitation/evaporation, albeit smaller, is not negligible. In terms of radiative fluxes at the top and surface in the RAD and EPR simulations, RAN differs much more from MRN than MAX does, showing that for this vertical resolution, the majority of the clouds appear more in contiguous layers than as independent layers.

Given the large sensitivity of both the model total cloud cover and surface and top-of-the-atmosphere radiation fields to the cloud overlap assumption used in the radiation and cloud scheme, it is very important that these quantities are not validated independently of each other, and of the radiative cloud overlap assumption. The cloud overlap assumption for precipitation processes should be made consistent with that for radiation.

1. Introduction

Although some assumptions on the vertical overlapping of cloud layers are always present in any computation of the radiation fields for a model producing fractional cloudiness in model levels, there have been in the past very few attempts at studying the impact of the different possible cloud overlap assumptions (COA) on the results of a general circulation model (GCM). While a change in cloud overlap assumption has been present in some sensitivity studies [e.g., Cubasch (1981), Geleyn et al. (1982), Morcrette and Geleyn (1985), Morcrette (1990), limiting only to work carried out with the European Centre for Medium-Range Weather Forecasts (ECMWF) model], it is generally accompanied by a revision to other parts of the radiation transfer package, in particular to cloud optical properties. Recently, Jakob and Klein (1999a) have looked at the role of the cloud overlap assumption on moist processes by comparing, for each model grid box, one time step diagnostics of precipitation/evaporation from the operational ECMWF cloud scheme with what would be produced by an ensemble of columns in which layer elements over the vertical can only be fully clear or cloudy, the so-called box-type approach. Their diagnostics showed large differences between the detailed and the operationally parametrized outputs of the moist processes.

One reason for the little interest shown to this problem is that the COA is an element usually deeply embedded in the radiation parametrization. In the absence of comprehensive information on the three-dimensional distribution of the cloud characteristics (geometry, ice/liquid water content, microphysics and related fields), the "tuning" of the cloud parameters to ensure a reasonable agreement of the model-produced radiation budget at the top of the atmosphere (TOA) with satellite observations has, in the past, been performed with the COA considered as internal to the radiation scheme. A full knowledge of the three-dimensional cloud distribution should be considered as external to the radiation scheme as, say, the surface radiative properties. Moreover, it is only recent that the validation of a model-produced total cloud cover is carried out in conjunction with the validation of the TOA radiative fluxes.

In the past, the COA could only be changed following

Corresponding author address: Dr. Jean-Jacques Morcrette, ECMWF, Shinfield Park, Reading, Berkshire RG2 9AX, United Kingdom.
E-mail: Jean-Jacques.Morcrette@ecmwf.int

either a major technical refurbishing of the radiation scheme or many extra computations previously incompatible with a GCM-oriented study. For example, the assumption of a random overlap of cloud layers has often been used in the past (e.g., Fouquart and Bonnel 1980) as it leads to simpler and computationally more efficient formulation. Because it was based on computations of fluxes for all possible combinations of layers, Morcrette and Fouquart's (1986) study of the effects of different COAs on the shortwave fluxes and heating rates was limited to one-dimensional computations on specified profiles with only three layers of clouds and to one-time-step simulations with a full GCM.

The most common COAs in the radiation schemes presently used in GCMs are the random, the maximum-random, and the maximum overlap assumptions (hereafter referred to as RAN, MRN, and MAX), none of which is completely justifiable on a global scale from limited observations of the actual atmosphere. Tian and Curry (1989) have tested the validity of the various COAs by applying them to the U.S. Air Force 3DNEPH (three-dimensional nephanalysis) in January 1979 over the North Atlantic Ocean. This dataset is still believed to be the best available information on the vertical distribution of clouds as it integrates both satellite and conventional observations over a relatively data-rich area. They compared the observed total cloud amount to the computed total cloudiness obtained with the different overlap assumptions. Their conclusion is somewhat in favor of the maximum-random overlap assumption first proposed by Geleyn and Hollingsworth (1979): Adjacent levels containing cloud are combined by using maximum overlap to form a contiguous cloud. Random overlap of discrete cloud layers, separated by clear sky, performed the best, although this assumption results in a systematic underestimation of the total cloud cover for the large horizontal resolutions, (200–500 km)^2, currently used in climate-oriented GCMs. More recently, Charlock et al. (1994) applied different interpretations for cloud overlap and cloud thickness to International Satellite Cloud Climatology Project (ISCCP) data and computed the resulting distribution of longwave (LW) radiative fluxes and cooling rates. With their top of the atmosphere radiation constrained by the data, they showed the high sensitivity of the atmospheric and surface LW radiation to the choice of cloud interpretation. On a related question, Wang and Rossow (1995) studied the cloud vertical structure and occurence of multiple-layered clouds from radiosounding observations.

As for the impact on models, Stubenrauch et al. (1997) discussed the effects on the radiation budget of implementing horizontal fractional cover and subgrid vertical structure for clouds within the Goddard Institute for Space Studies (GISS) climate model. This is, in essence, not very different from what has been done in the ECMWF model since 1981. Liang and Wang (1997) tested the impact on the Global Environmental and Eco-

logical Simulation of Ecological Systems GCM of a mosaic treatment of cloudiness, in which each grid box is subdivided and radiation is computed for all subgrids after accounting for a specified cloud overlap assumption. Wang and Rossow (1998) studied the effects on the atmospheric circulation of the GISS GCM of specifying various cloud vertical structures. All these experiments performed with low vertical resolution models indicate that changing the vertical radiative heating/cooling profile through a modification of the vertical distribution of the cloud layers has a large impact on the model radiation fields and simulated circulation.

In preparation for the operational implementation in September 1991 of a higher-resolution version of the ECMWF forecast model (from T106 to T213 horizontal resolution, and from 19 to 31 vertical levels), the ECMWF radiation scheme (Morcrette 1991) was modified, and the maximum and maximum-random assumptions were added to the existing random cloud overlap assumption, without any noticeable loss in the efficiency of the radiative calculations. Since that date, the radiative computations in the operational forecasts are performed with the maximum-random cloud overlap assumption.

This paper reports results of simulations obtained with the operational radiation scheme including either the RAN, the MAX, or the MRN cloud overlap assumption, within both the framework of the one-dimensional version of the ECMWF physics parametrization, and that of the three-dimensional model (RAD simulations). As important as the changes in cloud radiative forcing can be, they are only one element in what contributes to the energy distribution in the atmosphere. Another element is the heating/cooling due to the precipitation/evaporation processes linked to the presence of cloud layers. As the prognostic cloud scheme of Tiedtke (1993) explicitly links the formation, persistence, and dissipation of cloud water and volume to the various physical processes, we also introduced the various COAs within the cloud scheme following Jakob and Klein (1999b, hereafter JK) and studied the influence of the various COAs on the precipitation and evaporation fluxes due to the cloud processes. The evaporation–precipitation–radiation (EPR) simulations therefore include the effect of the various COAs in both the radiation and prognostic cloud schemes, whereas the evaporation–precipitation (EP) simulations only consider the effect within the cloud scheme, with the radiation fields computed with the operational MRN cloud overlap assumption.

Section 2 briefly presents the different cloud overlap assumptions and results of one-dimensional radiative computations for fixed vertical distributions of clouds. Appendix A presents the modifications to the radiation scheme, whereas appendix B discusses the implementation of the various COAs in the prognostic cloud scheme. The methodology of the three-dimensional experiments with the ECMWF model is then presented in

section 3. The response of the model to the change in COA is documented in section 4 from sets of winter 1987/88 simulations using realistic distributions of the sea surface temperature (SST), and for the prognostic cloud scheme of Tiedtke (1993). Finally, the robustness of the results in relation to change in the model horizontal or vertical resolution and the importance of the COA with regard to the strategy to be used for model validation are discussed in section 5.

2. Cloud overlap assumption: One-dimensional radiative computation

In a model simulation of the cloud and radiative fields, we are interested not only in the total cloud cover and radiation as viewed from the top of the atmosphere or the surface, but also in the vertical profile of these quantities. Therefore the definition of the different COAs is given from the point of view of the cloudiness CC_{IJ} encountered between any two levels I and J in the atmosphere. Note that in this discussion, cloudiness is the horizontal area covered by clouds. Clouds at individual layers are assumed to completely fill the vertical extent of the model layers such that the cloud volume fraction equals the cloud area fraction.

Let C_K be the cloud fraction of layer K located between levels K and $K + 1$; the maximum overlap assumption gives

$$CC_{IJ} = \max(C_I, C_{I+1}, \ldots, C_{J-1}),$$

the random overlap assumption gives

$$CC_{IJ} = 1 - \prod_{K=I,J-1} (1 - C_K),$$

and the maximum-random overlap assumption gives

$$CC_{IJ} = 1 - \prod_{K=I,J-1} \left\{ \frac{[1 - \max(C_K, C_{K-1})]}{1 - C_{K-1}} \right\}.$$

These three different COAs are illustrated in Fig. 1.

Results of one-dimensional radiative computations are presented first to confirm the validity of the modifications made to the radiation scheme to allow the handling of the different cloud overlap assumptions, and second to illustrate the direct impact of a change in COA on the radiative profiles.

The radiative fluxes and heating/cooling rate profiles are computed for a standard midlatitude summer atmosphere (McClatchey et al. 1972), with a surface shortwave (SW) albedo $\alpha_s = 0.175$ and a solar zenith angle of 23.5° corresponding to noon insolation at 45°N on 15 July, close to the date that would maximize the differences in SW heating. Provision for the LW and SW optical properties of water, ice, and mixed-phase clouds is made in the radiation scheme. Ice cloud optical properties are derived from Ebert and Curry (1992). Water cloud optical properties follow Smith and Shi (1992) in the longwave and Fouquart (1987) in the shortwave. Pure ice clouds are assumed for temperature

below 250 K, pure water clouds for temperature above 273 K, and mixed-phase clouds are diagnosed from temperature following Matveev (1984).

One-dimensional calculations are performed for different cloud configurations often encountered in three-dimensional simulations. The first one corresponds to a typical convective system and includes a convective tower of fractional cover of 0.15 from 820 to 290 hPa topped by a stratiform anvil of cover 0.4 and 70 hPa thick. The second case includes three layers of stratiform cloud of cover 0.3 between 890 and 820 hPa (low level), 640 and 545 hPa (middle level), and 290 and 220 hPa (high level), respectively. The profiles of the cloud longwave, shortwave, and net radiative forcing for these two cases are presented in Fig. 2, left and right panels, respectively. The cloud forcing term is simply the difference between the heating obtained for the cloudy atmosphere minus the clear-sky heating.

As discussed in appendix A, the different COAs are treated exactly in the LW part and only approximately in the SW part of the radiation scheme. Therefore, the LW MRN and MAX results are essentially the same for case 1, and the same holds for the LW MRN and RAN results for case 2. In the SW, the agreement on the SW forcing profiles is also very good. As seen in Tables 1 and 2, some small discrepancies can be found in the fluxes at the boundaries, particularly in case 2 for the MRN and RAN SW fluxes. However, their amplitudes make them irrelevant to the conclusions of the study.

In the first case (see Fig. 2, left panels), the anvil produces a strong LW cooling whereas a relative heating is found in the rest of the convective tower below. Compared to MRN/MAX, the RAN LW shows a smaller cooling peak in the anvil, smaller heating below within the tower, and larger warming in the clear PBL. All these features are consistent with the larger effective cloudiness that the RAN assumption produces between any two cloudy layers. This larger effective cloudiness (i) prevents the radiation from the lower atmospheric layers from escaping to space, thus the heating in the PBL; (ii) decreases the possible radiative exchanges within the tower, thus the smaller radiative heating; and (iii) decreases the upward LW flux at the base of the anvil, hence the smaller LW divergence in the anvil. Similarly, a stronger SW heating is linked in RAN to the larger cloud fraction available to screen the downward radiation and to the more diffuse character of this radiation in the cloudy fraction of the column. Consequently a smaller amount of SW radiation is available below the cloud base and this translates into a relative cooling. The smaller heating of the anvil in RAN is linked to the smaller SW flux divergence through a larger upward radiation due to the increased reflection on the larger effective amount of lower-level clouds.

In the second case (see Fig. 2, right panels), each of the three stratiform cloud layers produces an LW cooling inside and an LW heating immediately underneath. Differences between MAX and MRN/RAN results are

(a) Maximum–Random Overlap
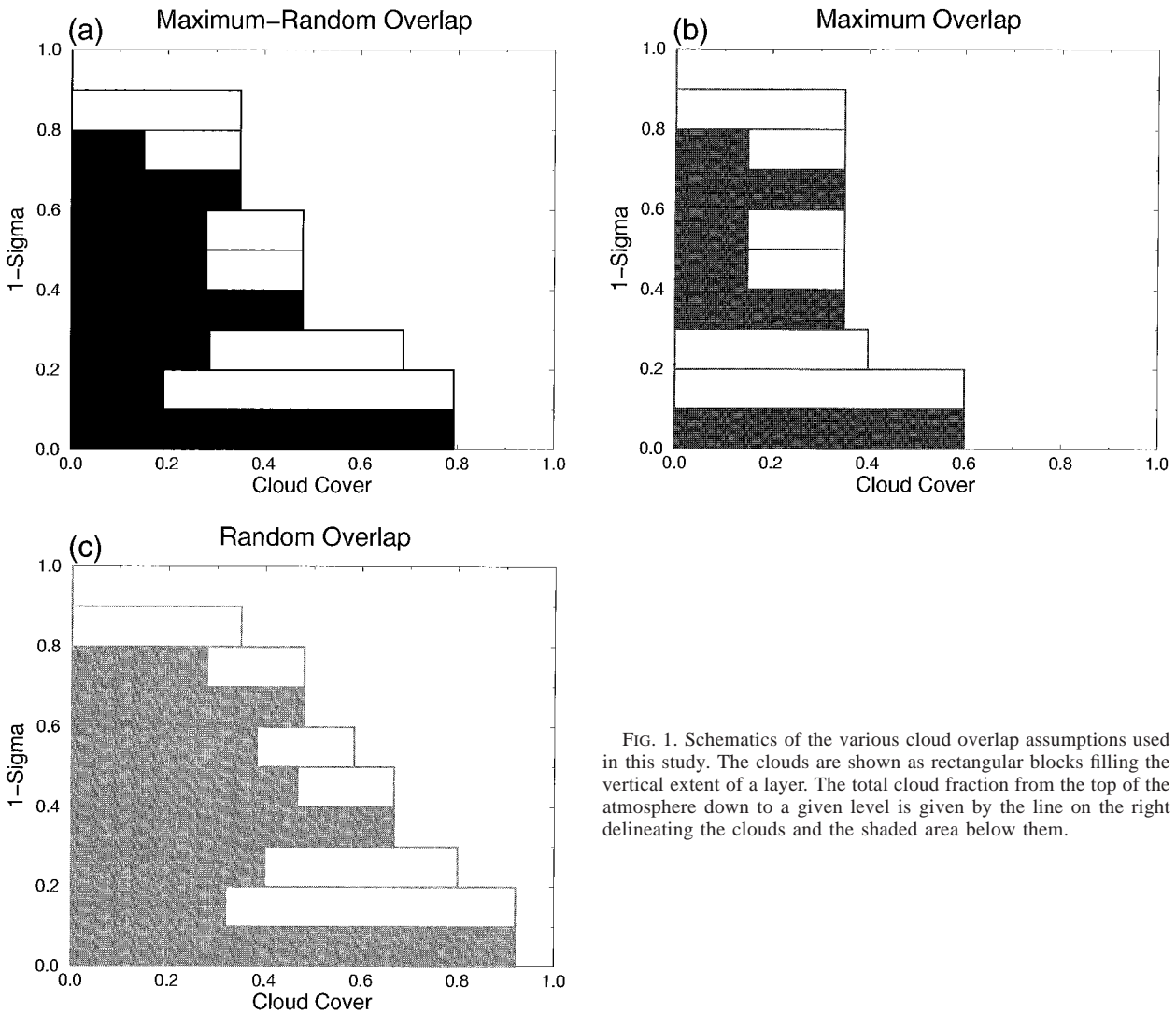

(b) Maximum Overlap

(c) Random Overlap

FIG. 1. Schematics of the various cloud overlap assumptions used in this study. The clouds are shown as rectangular blocks filling the vertical extent of a layer. The total cloud fraction from the top of the atmosphere down to a given level is given by the line on the right delineating the clouds and the shaded area below them.

consistent with the smaller total effective cloudiness given by MAX. The cooling in the low-level cloud is reduced in MAX because the middle- and high-level clouds prevent the radiation at the top of the low-level cloud from escaping to space. Similarly, the cooling in the high-level cloud is increased in MRN/RAN because the low- and middle-level clouds prevent the warmer radiation from the lower layers from reaching the base of the high-level cloud. The smaller total cloudiness in MAX also explains the smaller LW heating below the lowest cloud. In the SW, the difference in heating is very small within the clouds. The slightly larger relative cooling immediately below the clouds in MAX comes from the larger fraction of radiation being directly transmitted, as, in MRN/RAN, the radiation in the cloudy fraction of the column is more diffuse and therefore more likely to be absorbed. The smaller SW heating of the upper cloud with MRN/RAN is again linked to the increased reflection.

These one-dimensional computations show the validity of the treatment of the different COAs in the ECMWF radiation scheme. They also show the larger impact of a change of COA on the LW than on the SW radiative profiles.

3. Methodology of the sensitivity experiments with the ECMWF model

The model used in this study is the so-called cycle 18r6 version of the ECMWF forecast system, operational between 1 April 1998 and 8 March 1999, with some modifications to the precipitation/evaporation scheme discussed below. The recently revised physics package (Gregory et al. 1998) includes a revised radiation scheme accounting for a more accurate description of the water vapor continuum and ice cloud longwave optical properties consistent in both the longwave and shortwave parts of the spectrum, based on Ebert and
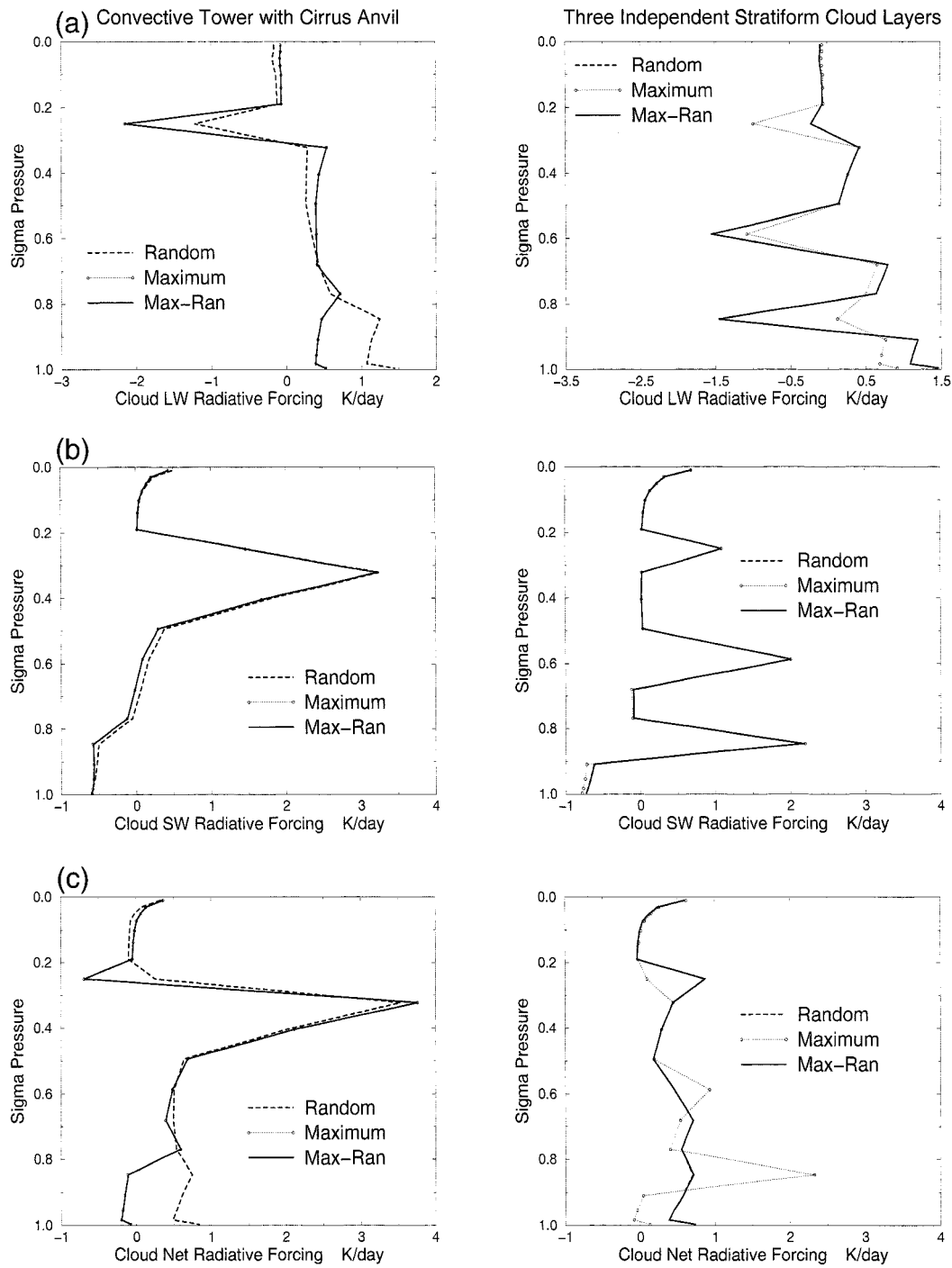
FIG. 2. The longwave (top), shortwave (middle), and net cloud radiative forcing (bottom) profiles for an atmosphere with an anvil-topped convective tower (left panels) and three independent stratiform cloud layers (right panels).

Curry (1992). The switching between deep or shallow convection was modified from a test on the moisture convergence to one based on the depth of the convection. Furthermore, the deep convective closure was changed from one based on moisture convergence (Tiedtke 1989) to one that relates the convection to the

reduction of the convective available potential energy toward zero over a certain timescale (Nordeng 1994). In the cloud scheme, after an inconsistency in the treatment of absorption of solar radiation had been removed, the original formulation of the fallout of cloud ice of Tiedtke (1993) was reintroduced in the model. The ver-

TABLE 1. Radiative fluxes at the top of the atmosphere and surface computed for different cloud overlap assumptions. Results are for a midlatitude summer (MLS) atmosphere including a typical convective cloud (see text), over a surface of albedo $a_s = 0.175$. TCC is the total cloud cover corresponding to the cloud overlap assumption. TTR and TSR are the net terrestrial and solar radiation fluxes at the top of the atmosphere, respectively. STR and SSR are the net terrestrial and solar radiation fluxes at the surface, respectively. LFT and SFT are the longwave and shortwave cloud forcings seen from the top of the atmosphere; LFS and SFC are the longwave and shortwave cloud forcings seen from the surface. All quantities except TCC are in W m^{-2}.

	TCC	TTR	TSR	LFT	SFT	STR	SSR	LFS	SFS
MAX	0.400	−249.8	901.3	36.3	−155.5	−66.1	649.6	12.2	−179.7
MRN	0.400	−249.4	901.3	36.7	−155.5	−66.0	649.6	12.2	−179.7
RAN	0.774	−216.2	860.6	70.0	−194.8	−45.8	602.8	32.5	−224.7

tical diffusion scheme is now called three times within each model time step, improving the accuracy of the surface drag coefficient. The dynamical part of the model includes the semi-Lagrangian scheme on a linear grid of Hortal and Simmons (1991) and Hortal (1998). The prognostic cloud scheme (Tiedtke 1993) represents both stratiform and convective clouds, and their time evolution is defined through two large-scale budget equations for cloud water content and cloud fractional cover. This scheme links the formation of clouds to large-scale ascent, diabatic cooling, boundary layer turbulence, and their dissipation to adiabatic and diabatic heating, turbulent mixing of cloud air with unsaturated environmental air, and precipitation processes. The results presented in the following sections are obtained with the scheme used operationally for global forecasts and analyses (Jakob 1994). It differs from Tiedtke's original formulation in two aspects: first, through a revised representation of the ice sedimentation after Heymsfield and Donner (1990), second, through a new precipitation/evaporation scheme (JK), which explicitly accounts for the vertical distribution of cloud layers and allows the cloud overlap assumption to be applied consistently with what is done for the radiative computations.

A number of different sets of T_L95 L31 experiments were run over November 1987 to February 1988 corresponding to the random, maximum-random, and maximum COAs. Each set includes six simulations starting 24 h apart from 26 November to 1 December 1987 and all finishing on 1 March 1988. All simulations are performed with the SST varying according to the observed SST at the time. Such ensembles of experiments have been shown by Brankovic et al. (1994) to be large enough to give a reasonable level of statistical significance. The first set, hereafter referred to as RAD, has the various cloud overlap assumptions used only in the radiation scheme. The second set, EPR, has the various COAs implemented in both the radiation and the prognostic cloud schemes, so that the effect of the various

COAs is also felt in the computations of the large-scale precipitation and evaporation (see appendix B). The third set, EP, only considers the effect of the COAs within the prognostic cloud scheme, but has the radiation computed assuming the operational maximum-random cloud overlap assumption. In the following (Figs. 4, 6, 8, 9, 12–20), results are usually compared in terms of the impact of the COA by comparing MAX and MRN (left panels) and RAN and MRN (right panels) when the change in COA is applied to radiation only (top panels: R), to radiation and evaporation/precipitation (middle panels: EPR), or to evaporation/precipitation only (bottom panels: EP). The "reference" is always the operational configuration, which includes the MRN COA and EPR. In all the above-mentioned figures, R11 and EP11 are, by definition, identical to EPR11.

4. Results

a. Cloudiness

We first study the impact of changing the COA in the radiation and precipitation/evaporation schemes (EPR simulations). Figure 3 presents the total cloudiness (TCC) averaged over the last three months (December–January–February, DJF) of the EPR simulations with the MRN, MAX, and RAN COAs. Table 3 presents the globally averaged total cloudiness. Not surprisingly, the set of MAX simulations display the minimum total cloud cover at 0.609, followed by the MRN at 0.639, whereas the RAN simulations have a much larger total cloud cover at 0.714. The increase from MRN to RAN (respectively, the decrease from MRN to MAX) is apparent over most of the globe, but is more pronounced over the subtropics, particularly those of the Southern Hemisphere, as seen in the middle panels of Fig. 4. A very similar response to the one found for EPR is found in the RAD simulations, as can be seen in comparing

TABLE 2. As in Table 1 but for an MLS atmosphere including three overlapping high-, mid- and low-level clouds (see text).

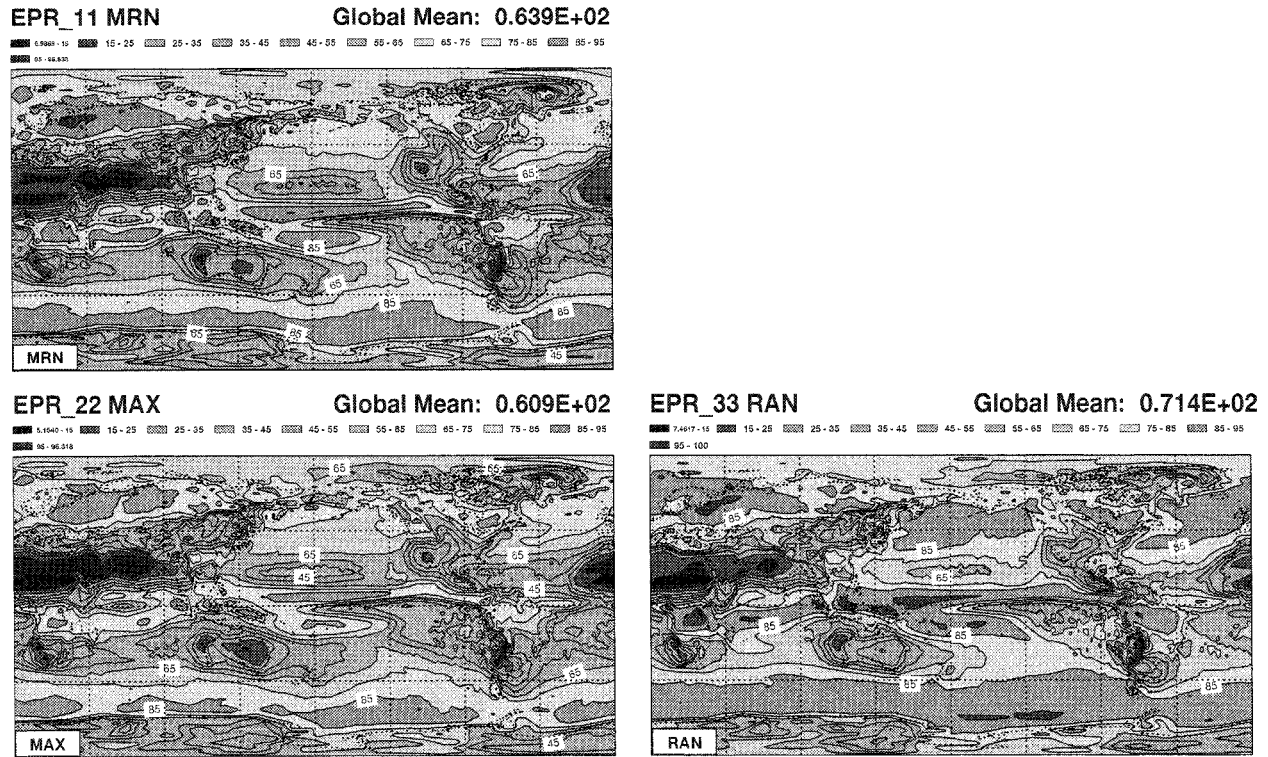|	TCC	TTR	TSR	LFT	SFT	STR	SSR	LFS	SFS
MAX	0.300	−251.3	896.9	34.8	−159.9	−59.4	639.4	18.9	−189.9
MRN	0.657	−238.4	875.4	47.7	−181.4	−48.5	618.0	29.8	−211.3
RAN	0.657	−238.4	873.0	47.7	−182.3	−48.5	615.4	29.8	−212.1

FIG. 3. TCC averaged over the last three months (DJF) of the RAD simulations with the MRN, MAX, and RAN cloud overlap assumption (COA). Step is 10% starting from 5%.

the top and mid panels of Fig. 4. Most of the effect on cloudiness is linked to changes in the vertical arrangement of clouds within the radiation scheme rather than to the effects of this arrangement for the precipitation/evaporation processes. This can be concluded from the much smaller impact on TCC brought by the various COAs in the EP simulations (bottom panels of Fig. 4). However, the global differences RAN–MRN and MAX–MRN are slightly larger in EPR than in RAD, indicating that the various COAs actually have an effect also on the precipitation/evaporation processes, which is to amplify somehow the main signal brought by the radiative processes.

Are these changes simply reflecting the different geometrical distribution of the cloud elements on the vertical or are they linked to actual changes in the volume of the cloud elements? A simple check whether the

cloud volume is actually modified is obtained by diagnosing the total cloud cover for all sets of simulations and applying the operational maximum-random overlap assumption to the various cloud elements. Global results for this MRN-equivalent total cloud cover are also given in Table 3. Here it must be noted that the total cloud cover computed under the TCC heading is based on cloud fields archived every 24 h, whereas the MRN-equivalent total cloud cover is computed from cloud fields available at every time step (3600 s). The difference for all configurations is at most 0.002 and is obvious in the MRN column. Results in the other columns also include this slight inconsistency. Figure 5 presents the MRN-equivalent TCC for the EPR experiments. The differences RAN–MRN and MAX–MRN for the three sets RAD, EPR, and EP are shown in Fig. 6. The first result is that most of the change in TCC is not reflected

TABLE 3. The global mean of the total cloudiness for various configurations. TCC refers to the cloudiness actually seen by the model, whereas MRN is a diagnostic computed assuming a maximum-random overlapping of cloud layers. N.B.: TCC and MRN results for the MAX-RAN configuration are slightly different because TCC is computed from cloud fields sampled every 24 h whereas MRN is computed from cloud fields available at each time step (3600 s).

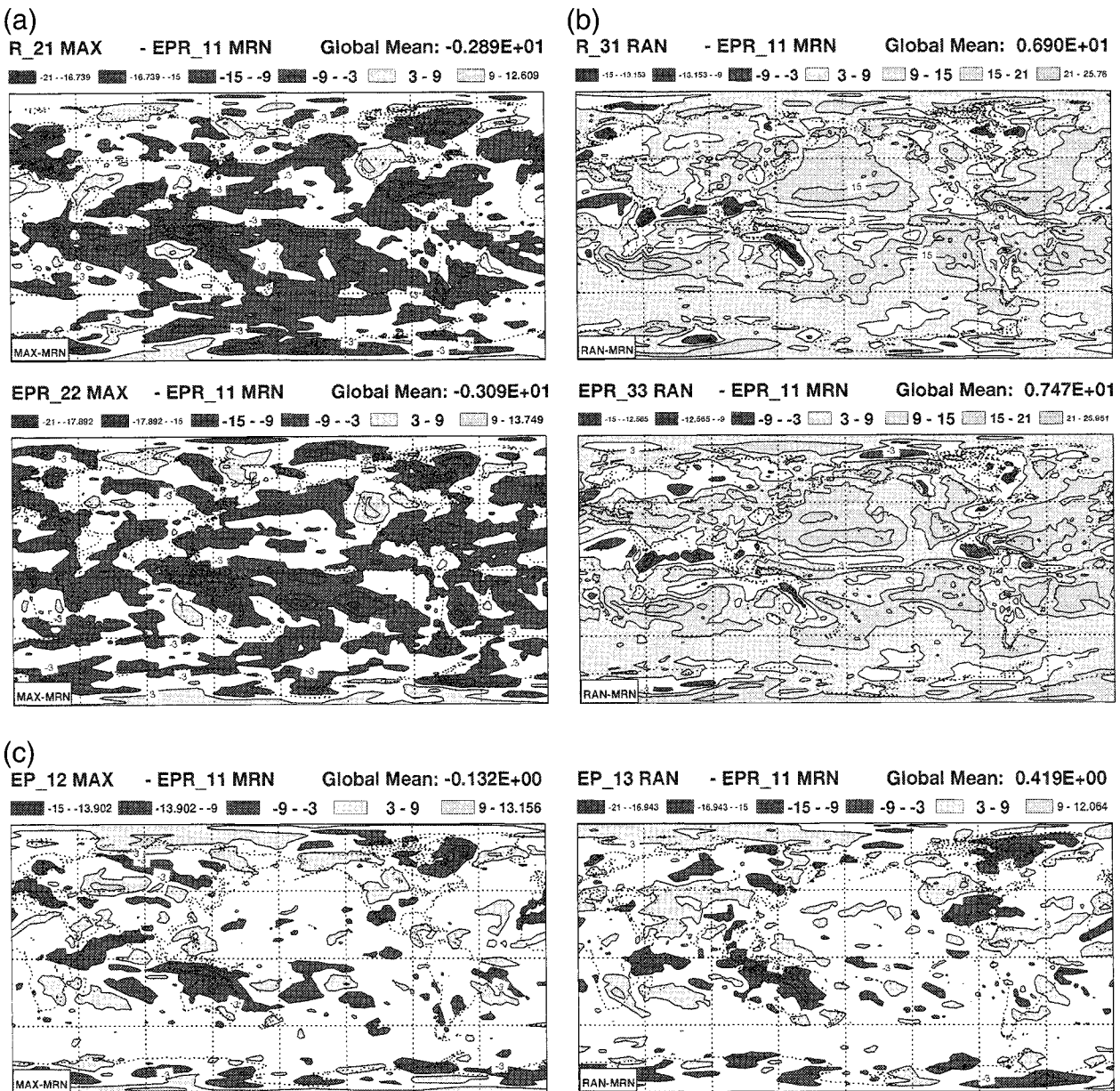|	Evaporation–precipitation–radiation			Radiation		Evaporation–precipitation	
	MRN	MAX	RAN	MAX	RAN	MAX	RAN
TCC	0.639	0.609	0.714	0.611	0.708	0.638	0.644
MRN	0.641	0.638	0.645	0.640	0.639	0.639	0.645

FIG. 4. Differences in TCC between MAX–MRN (left panels) and RAN–MRN (right panels) for the RAD (top), EPR (middle), and EP (bottom) simulations. Step is 6% starting from ±3%, with dark shading over negative and light shading over positive values.

in the MRN-equivalent TCC, showing that a large fraction of the signal is due to the geometrical overlapping in the radiation scheme. The RAD MRN-equivalent TCCs are now very similar, within 0.2% of each other. Second, the similarity between EPR and EP results for RAN–MRN and MAX–MRN now points toward the role of the COAs in the precipitation/evaporation processes of the cloud scheme in explaining the (second order) changes in the volume of the cloud elements.

Figure 7 presents the zonally averaged vertical distribution of the cloudiness in the EPR simulations, whereas Fig. 8 displays the differences MAX–MRN and RAN–MRN for the RAD, EPR, and EP simulations. Cloudiness in the intertropical region behaves similarly in RAD and EPR, with, for RAN–MRN, (i) an increase in the uppermost high cloudiness, corresponding to anvil cirrus cloud at the level of detrainment of the convection; (ii) a decrease on both sides of the maximum convection; and (iii) an increase in cloudiness underneath. All these features are consistent with a decreased stabilization of the atmosphere by clouds when RAN is used. For MAX–MRN, both RAD and EPR show an increase in the uppermost cloud in the Tropics, with a decrease below in the 200–400-hPa layer. The impact
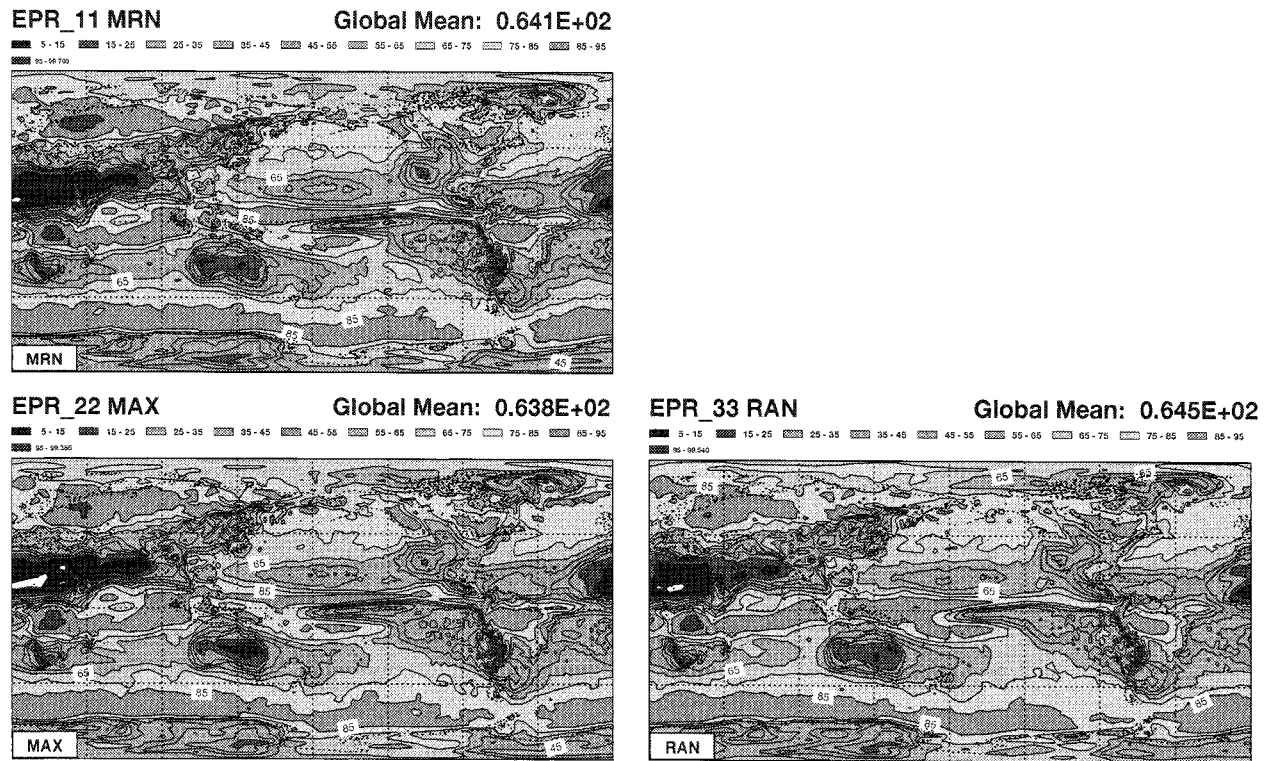
FIG. 5. The MRN-equivalent total cloudiness (see text) of the RAD simulations with the MRN, MAX, and RAN COAs. Step is 10% starting from 5%.

of MAX is much smaller than that of RAN, showing that, in the ECMWF model with 31 vertical levels, most of the cloudiness tend to be formed in contiguous layers, where the MRN overlap assumption already works as the MAX overlap assumption would.

At higher latitudes, the signal seen in RAN–MRN differs between RAD and EPR/EP, with an increase of cloudiness between 20° and 45°N, and 40° and 60°S, between 200 and 850 hPa in the EPR results, and between 30° and 50°N, and 20° and 70°S, between 200 and 800 hPa in the EP results. This increase in clouds follows an increase in relative humidity (higher specific humidity, no change or decrease in temperature; see sections 4d and 4e). Such an increase is not seen in the RAN–MRN RAD results.

b. Radiative fluxes and heating rates

In considering the impact on the radiative fluxes, it is not the cloud fraction or cloud volume, but the cloud volume together with the longwave emissivity and the shortwave optical thickness that matters. These two radiative quantitites obviously depend on the amount of condensed water in the clouds, and on the radiative properties (longwave absorption coefficient, and shortwave single scattering albedo, asymmetry factor, and extinction coefficient). Figure 9 presents the differences in longwave radiative heating for all sets of simulations.

Again, we see the similar response of the RAD and EPR simulations, compared to the EP simulations. RAN–MRN displays (i) an increased cooling in the upper part of the troposphere, with a heating underneath, more pronounced in the Southern Hemisphere; (ii) an increased cooling in the subtropics corresponding to the increase in the amount of low-level (stratocumulus and/or trade wind cumulus type) clouds; and (iii) a greenhouse warming below these clouds. The MAX–MRN results for RAD and EPR shows a midtroposphere warming and a cooling over most of the planetary boundary layer. Results of the EP simulations confirm the expected small effect on the radiative heating rates, with a little extra cooling where the cover by mid- to high-level clouds has increased.

Figures 10 and 11 present the outgoing longwave radiation (OLR) and the absorbed shortwave radiation (ASW) in the atmosphere for the EPR MRN and RAN simulations. While the global means presented in Table 4 would all appear in reasonable agreement with global averages from observations such as the Earth Radiation Budget Experiment (ERBE), Figs. 10 and 11 clearly show the overly large impact of clouds in the ITCZ (related to ERBE) when the RAN assumption is used in the radiation scheme. Figures 12 and 13 show the differences of OLR and ASW relative to MRN for all configurations, and this problem stems from the radiative processes as the EP simulations does not display the signal. For the RAD
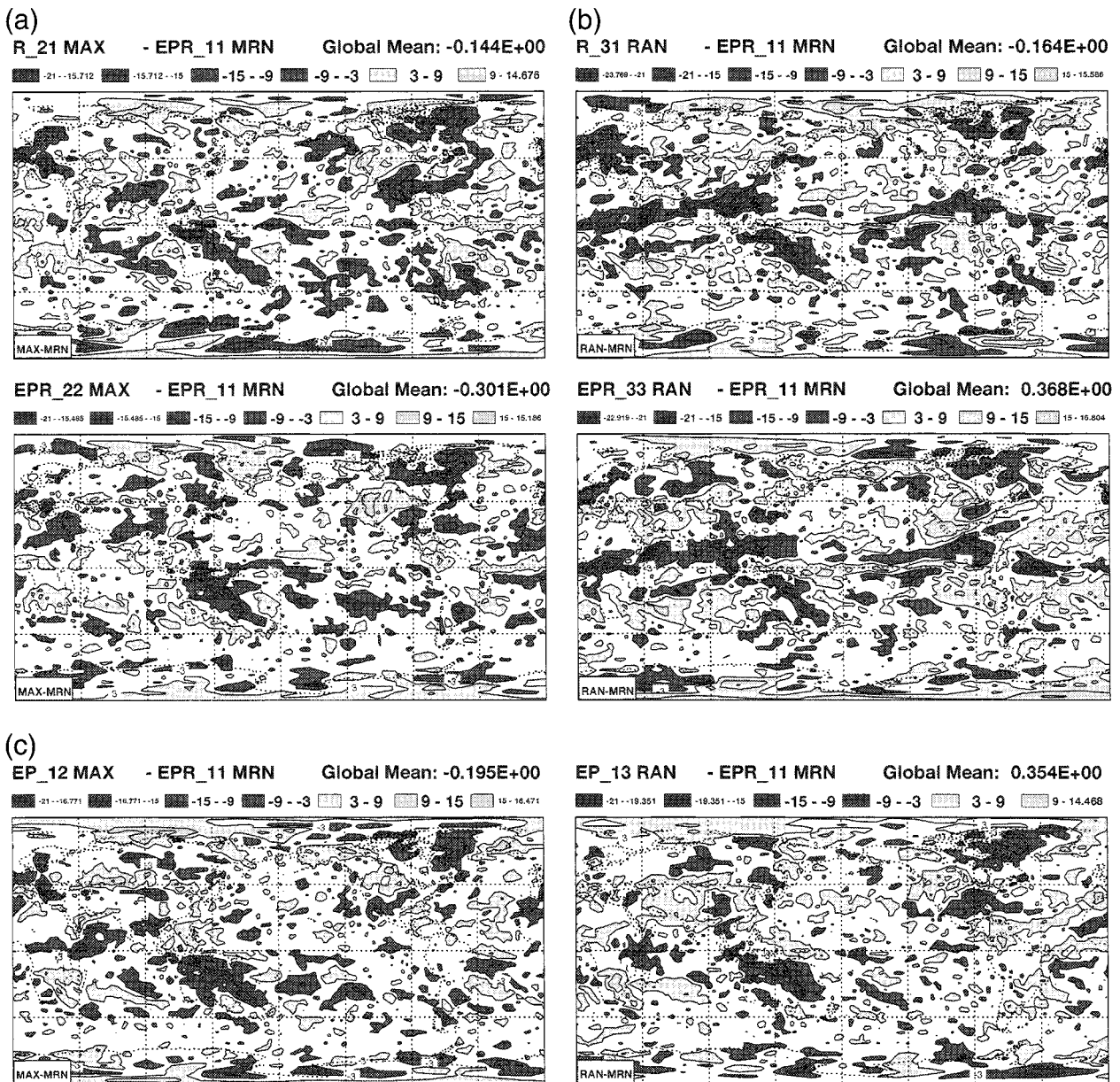
FIG. 6. Differences in MRN-equivalent total cloud cover (in %) between MAX–MRN (left panels) and RAN–MRN (right panels) for the RAD (top), EPR (middle), and EP (bottom) simulations. Step is 6% starting from ±3%, with dark shading over negative and light shading over positive values.

and EPR simulations, over the ITCZ, both the OLR and ASW go down to too low values, with averaged OLRs over the three-month period reaching 160 W m^{-2} around 150°E, and averaged ASWs reaching 200 W m^{-2}. However, results in section 4a indicate that, at least for the ECMWF model with its prognostic description of clouds, it would be rather artificial to decrease the volume of clouds to ensure a smaller total cloud cover in the ITCZ, which would lead to OLR and ASW closer to observations. At least, over the ITCZ, the present parametrizations for cloud cover, water, optical properties, and ra-

diation transfer cannot reproduce correctly the TOA (and surface) radiation fields, cloud horizontal and vertical extent, and vertically integrated cloud water. In this respect, the EPR (and RAD) configurations are simply doing less badly than RAN.

c. Precipitation

Figure 14 presents the solid and liquid precipitation fluxes, as diagnosed within the cloud scheme, for the different configurations. These fluxes are produced by
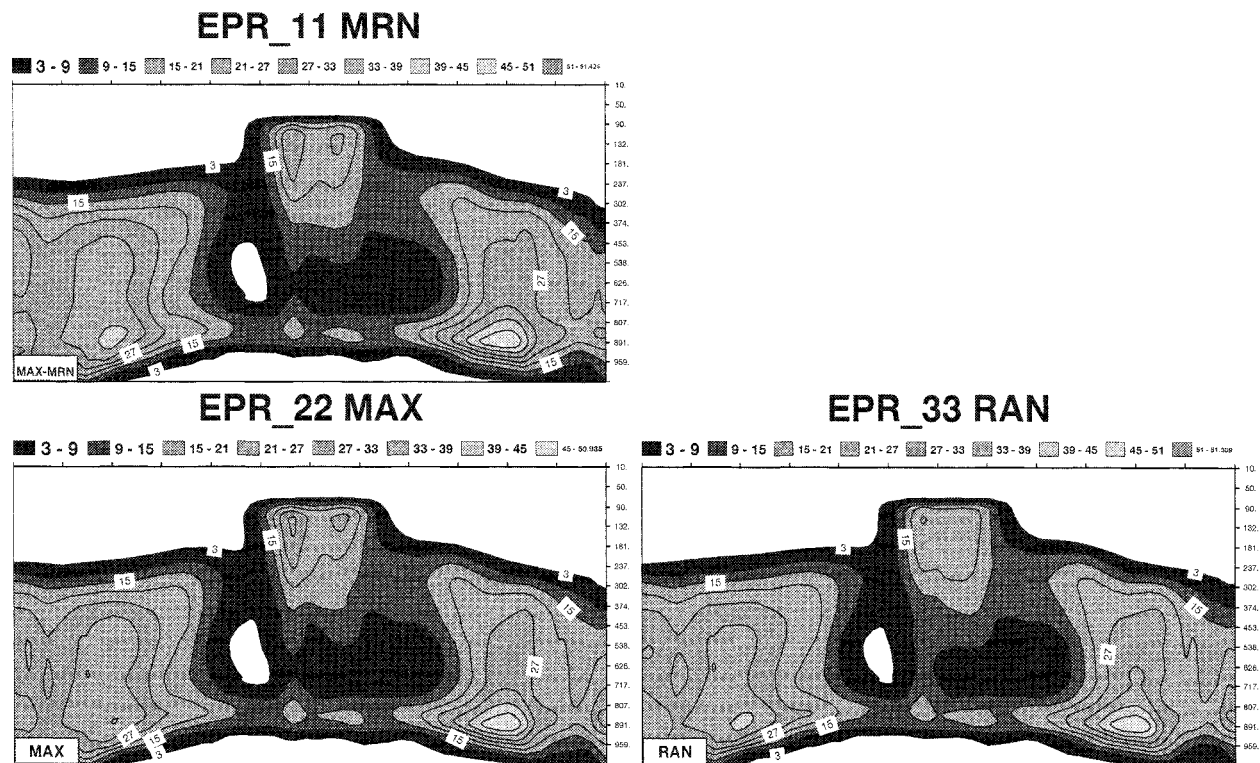
FIG. 7. The zonally averaged vertical distribution of cloudiness in the EPR simulations. Step is 6% starting from 3%.

the large-scale processes handled by the cloud scheme and do not include the convective precipitation produced by the mass-flux scheme (for which the COA has no direct effect). RAD and EPR results are very similar, both sets of simulations showing an increase in both the solid and liquid precipitation, in the atmospheric layers corresponding to middle-level clouds for the snow precipitation flux (above the thick line, indicating the freezing level diagnosed from the zonally averaged temperature), and below the freezing level for the liquid precipitation flux (below the thick line). However, although the overall pattern is similar, the details are different with the increase in snow precipitation in the equatorial region larger in EPR than in RAD, and similar behavior in the midlatitudes of both hemispheres. For the liquid precipitation flux, the pattern is different, with the decrease in the equatorial region and the Southern Hemisphere larger in RAD than in EPR simulations. MAX–MRN displays almost the reverse signal with respect to RAN–MRN, for both the solid and liquid precipitation fluxes. For the EP simulations, the amplitude, albeit nonnegligible, is much smaller, showing again that the impact of the COA on the radiative processes dominates that of the precipitation/evaporation processes.

In terms of geographical patterns, despite the size of the sets (comprising six experiments each), the changes are much more variable with both the configuration (RAD, EPR, or EP) and the COA (MRN, MAX, RAN). Figure 15 compares the total precipitation for the var-

ious configurations. Globally averaged, the impact of the various COAs is similar in RAD and EPR, with a decrease in total precipitation going from MRN to MAX, and an increase going from MRN to RAN. The reverse trend is seen for the EP configuration. Most of the effect is seen within the band 10°N–40°S and is related to the zone where the Hadley circulation has most influence for the season (DJF). RAD and EPR show an increased (decreased) precipitation on the equator over the Indian Ocean and west Pacific going from MRN to RAN (from MRN to MAX). For EP simulations, the change is more difficult to ascertain.

d. Cloud precipitation/evaporation and specific humidity

Figure 16 presents the difference in snow and rain evaporation, as diagnosed within the cloud scheme, for the different configurations. Contrary to precipitation (see Fig. 14) whose onset depends on the destabilization of the layer, and therefore on the temperature profile and the radiative cooling profile, evaporation depends more on the clear-sky fraction underneath the precipitating cloud. Thus, EP and EPR results are much more similar, with RAD being the odd one out. However, both the evaporation of the snow and rain produced by the (large scale) cloud scheme are small terms in the moisture budget, and the pattern of relative change in specific humidity (Fig. 17) is more strongly influenced by the
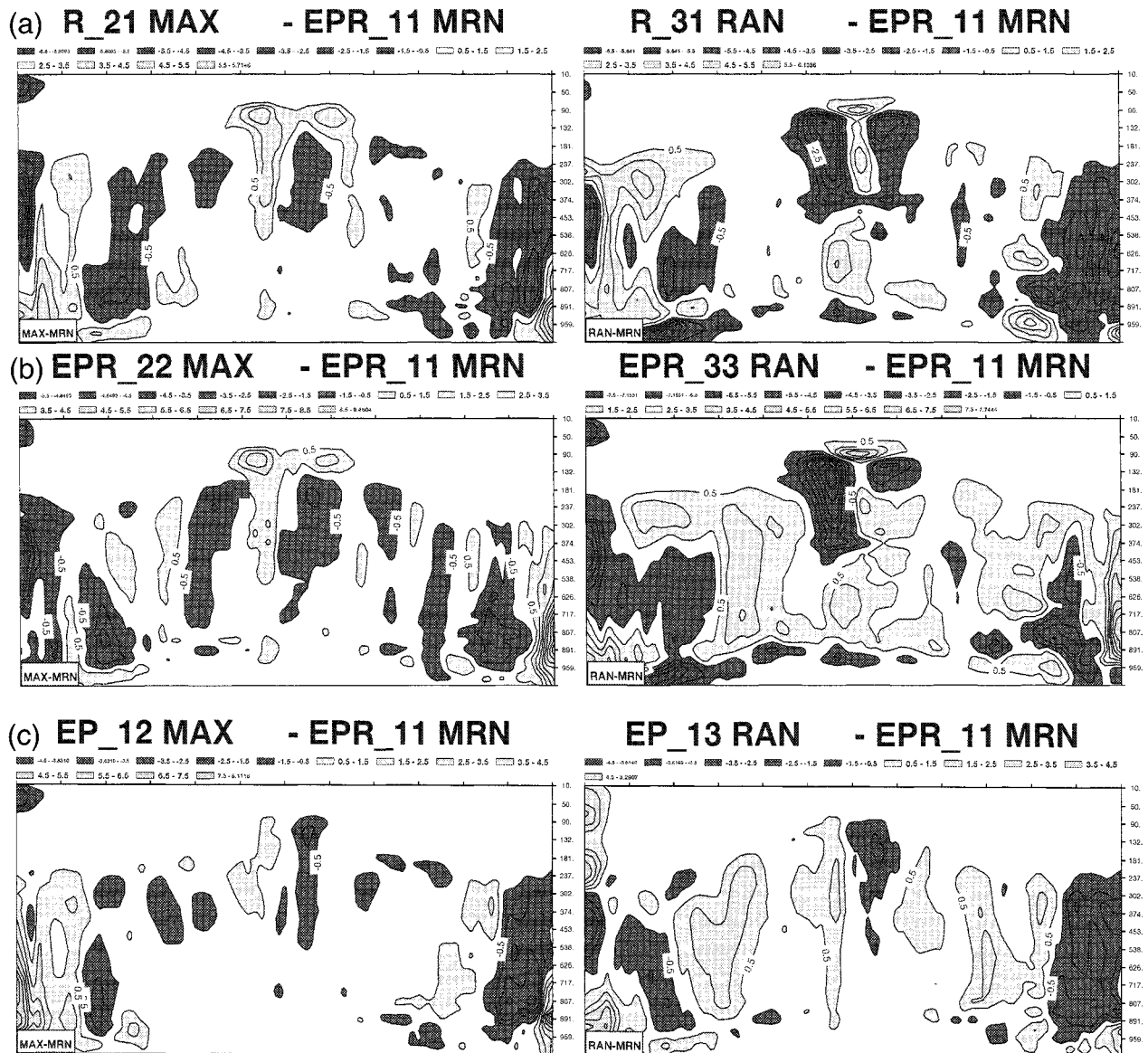
FIG. 8. Differences in zonally averaged vertical distributions of cloudiness between MAX–MRN (left panels) and RAN–MRN (right panels) for the RAD (top), EPR (middle), and EP (bottom) simulations. Step is 1% starting from ±0.5%.

COA for radiation than that for precipitation/evaporation. Here the main factor in the change in specific humidity is the corresponding change in temperature (see section 4e), as the impact on relative humidity (not shown) is much smaller. This is also related to the collection of droplets in underlying clouds being a more efficient process than the evaporation of precipitation in the underlying layer clear-sky fractions, and this is independent of the COA. In all cases, relative to MRN, MAX induces an atmospheric drying over most of the troposphere at all latitudes except the northernmost, whereas RAN induces a moistening over most of the troposphere.

e. Temperature

Figure 18 presents the difference in zonally averaged temperature for all three sets of simualtions. Results for RAD and EPR are similar with an increase in temperature below 100 hPa between 30°N and 45°S, and decrease higher up. This effect is linked to the more radiatively effective anvil clouds topping the convective areas, which act as a lid for escaping LW radiation, and hence contributing to some greenhouse warming underneath. MAX–MRN corresponds to a smaller cooling. All simulations also display a large warming over the whole depth of the Arctic atmosphere. With the excep-
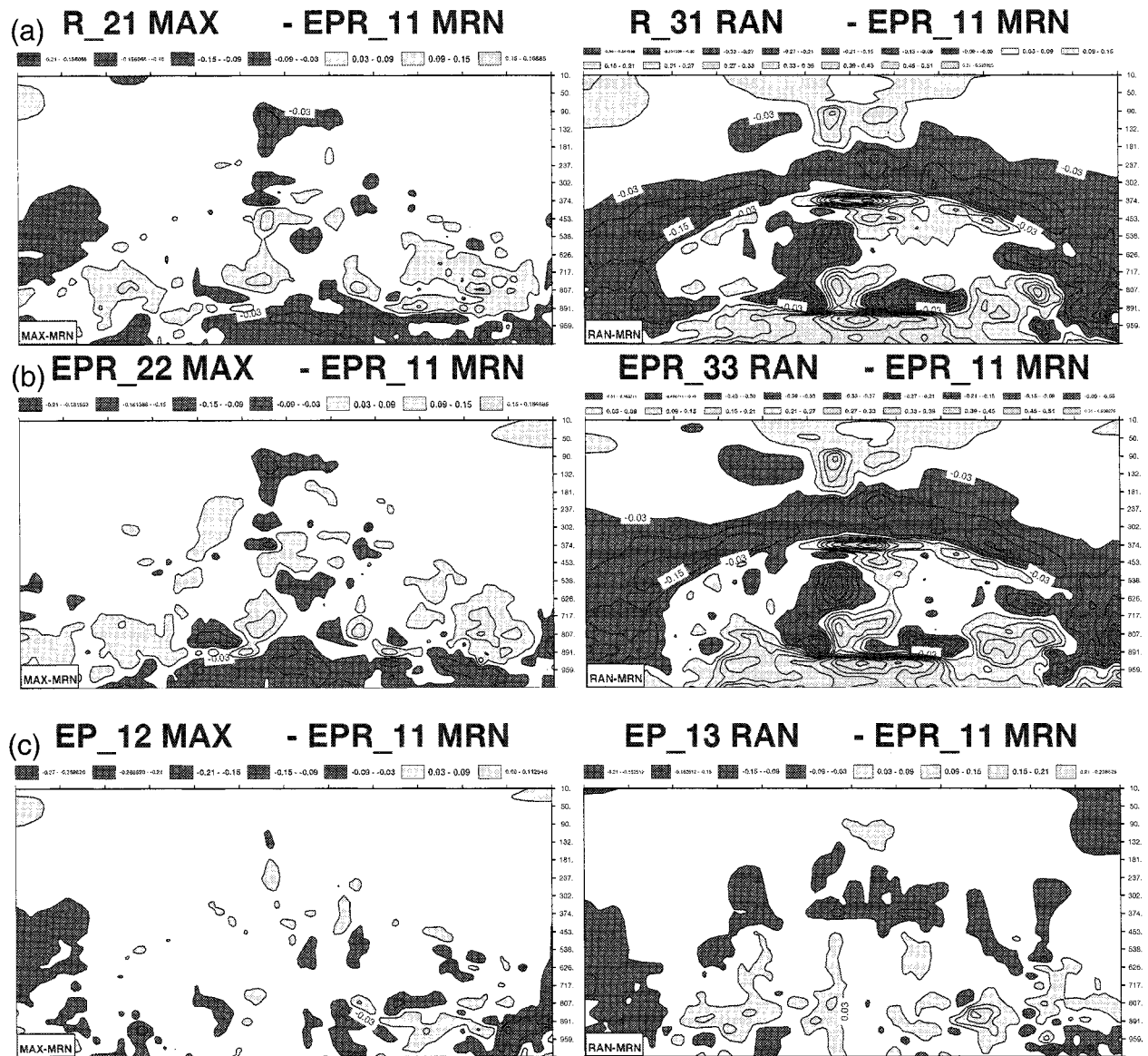
FIG. 9. Differences in zonally averaged vertical distribution of longwave heating rate (per day), between MAX–MRN (left panels) and RAN–MRN (right panels) for the RAD (top), EPR (middle), and EP (bottom) simulations. Step is 0.06 K day^{-1} starting from ± 0.03 K day^{-1}.

tion of the last one, for which a Student's t-test indicates a statistical significance below 0.9, the signals discussed above are linked to the effect of the overlap assumption within the radiation scheme, as contrasted by the EP results that show almost no effect within the lower tropical atmosphere, and a small cooling at higher latitudes.

f. Global mean hydrological cycle

Figure 19 presents the globally averaged hydrological cycle for the EPR MRN simulation, averaged over the last three months of the integrations. Table 6 compares the individual terms for all configurations. The notation

follows Tiedtke (1993). There are several notable features in Table 6. For both radiation and precipitation/ evaporation the differences between RAN and MRN are larger than those between MAX and MRN, a feature already pointed out above. The largest overall impact on the hydrological cycle arises from the introduction of the RAN assumption into the radiation scheme. Particularly it is the COA configuration that induces a larger atmospheric water vapor content in RAN than MRN or MAX, reflecting an intensified Hadley circulation with RAN compared to MRN or MAX.

When the change in COA is seen by the radiation scheme (EPR and RAD simulations), this is linked to
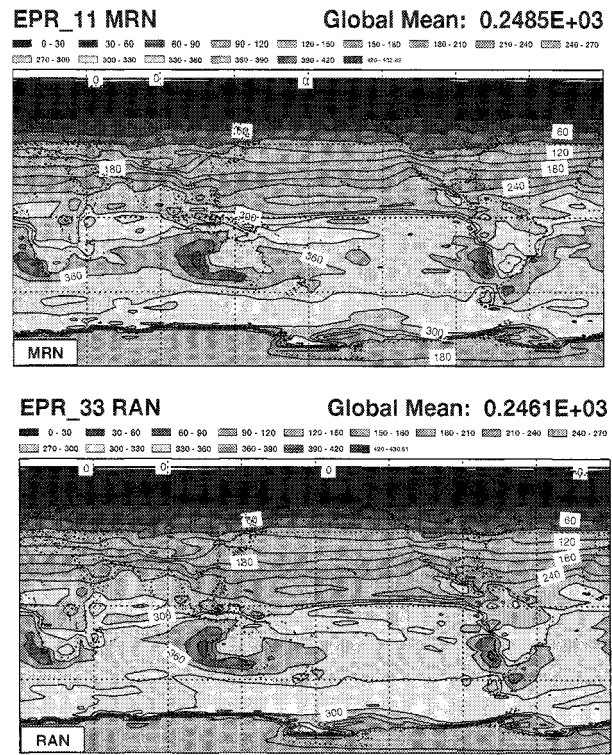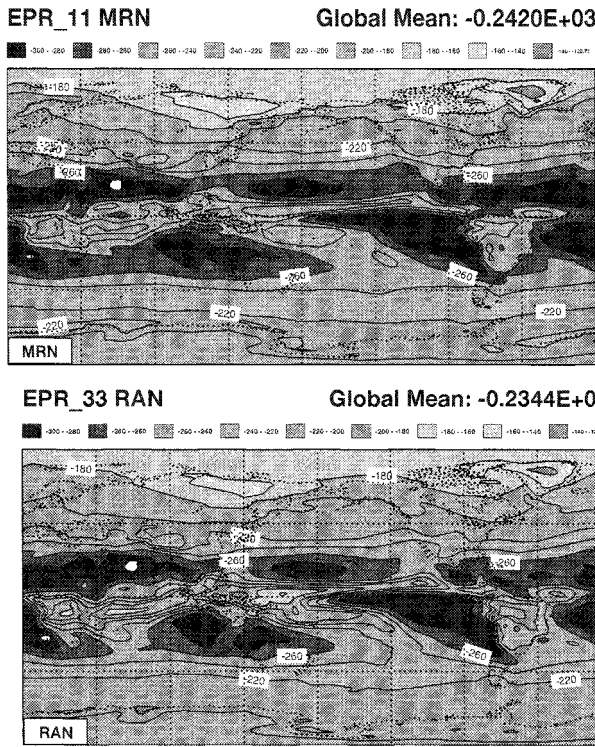
FIG. 10. The outgoing LW radiation at the top of the atmosphere (W m^{-2}) of the EPR simulations with the MRN, MAX, and RAN COAs. Step is 20 W m^{-2} starting from 120 W m^{-2}.

FIG. 11. The absorbed SW radiation in the atmosphere (W m^{-2}) of the EPR simulations with the MRN, MAX, and RAN COAs. Step is 30 W m^{-2} starting from 0 W m^{-2}.

a larger latent heat flux [SLHF (in W m^{-2}) in Table 5 or F_S in Table 6]. This is related to the increase in surface downward LW radiation (shown as an increase in surface net LW flux, STR, in Table 6) and not to the change in downward SW radiation, which partly compensates for the change in STR brought by a larger total cloud cover. For the EPR and RAD simulations, when considering the large-scale cloud processes, the generation of precipitation (G_P), its subsequent eventual evaporation (E_P), and the amount of precipitation reaching the ground (P_L) are enhanced by RAN (decreased by MAX) relative to MRN. The equivalent terms related to the convective processes (G_P^c, E_P^c, P_C) all decrease when going from MAX to MRN to RAN, showing that part of the hydrological cycle is taken over by the large scale from the convective processes.

When the change in COA is seen by the precipitation/ evaporation scheme only (EP simulations), both G_P and E_P increase with RAN relative to MRN (as in the RAD and EPR simulations). However, the precipitation P_L reaching the ground is smaller, the increase in G_P not compensating that in E_P. On the contrary, G_P^c, E_P^c, and P_C increase going from MRN to RAN.

5. Discussion and conclusions

The overlapping of cloud layers in a atmospheric model has long been seen as a philosophical problem, inasmuch as whatever parametrization is used, it tries to represent a two-dimensional effect in what is, up to now, essentially a one-dimensional computation, be that of radiation or of precipitation/evaporation fields. Until recently, some large-scale models were still considering cloudiness as an all or nothing process, even though their horizontal resolution was corresponding to grid size of the order of 10^5 km^2. Observations showing that clouds have a U-shaped distribution, with occurrence most likely to be 0 or 1, should be considered with

TABLE 4. The components of the radiation budget at the top of the atmosphere. Unit is W m^{-2}.

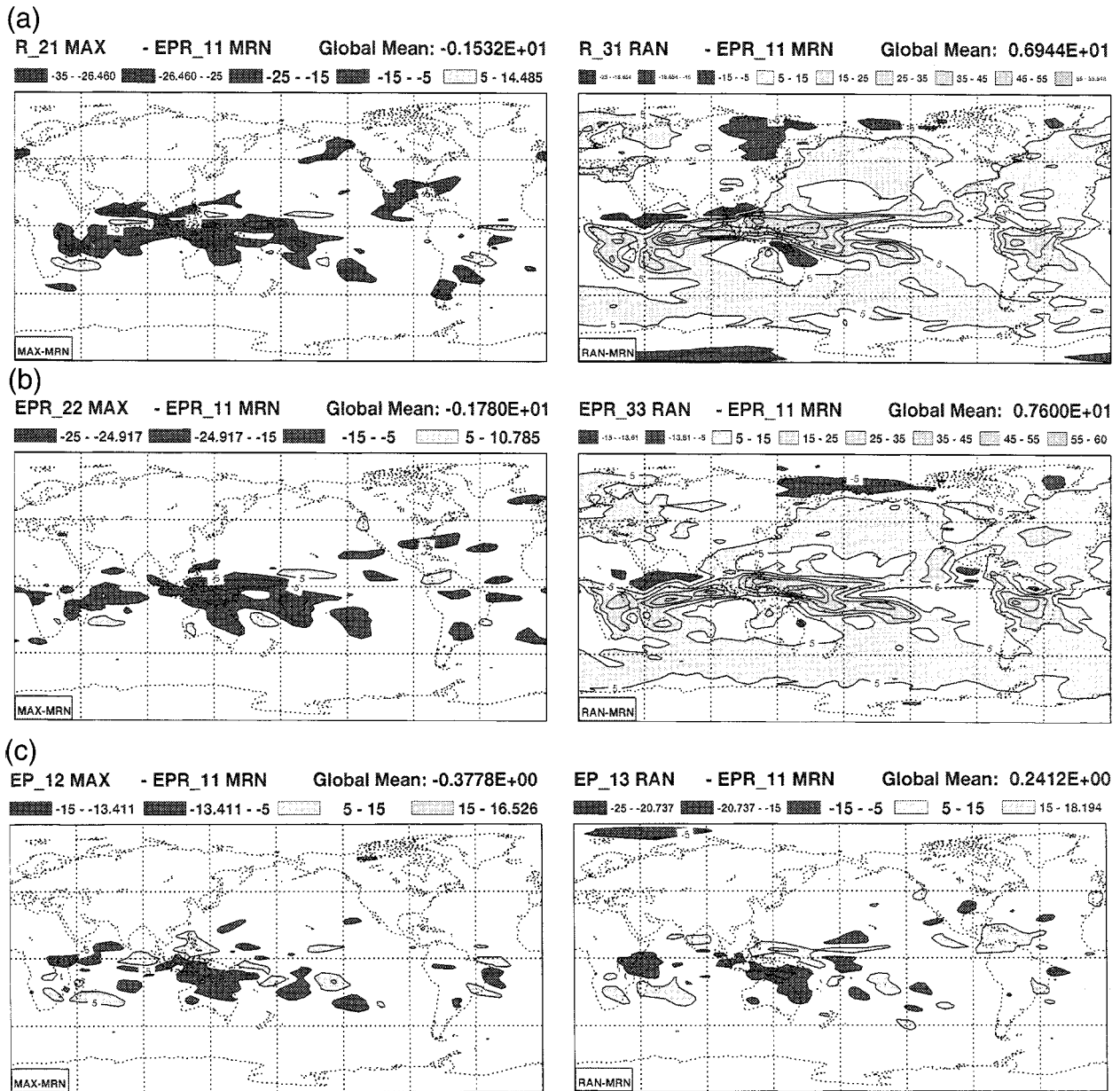|	Evaporation–precipitation–radiation			Radiation		Evaporation–precipitation	
	MRN	MAX	RAN	MAX	RAN	MAX	RAN
OLR	241.2	242.8	234.5	243.1	234.7	241.6	241.6
ASW	247.1	248.4	245.1	249.6	247.0	247.0	246.2

FIG. 12. Differences in outgoing LW radiation at TOA (W m^{-2}), between MAX–MRN (left panels) and RAN–MRN (right panels) for the RAD (top), EPR (middle), and EP (bottom) simulations. Step is 10 W m^{-2} starting from ± 5 W m^{-2}.

respect to the spatial and temporal scales actually described by numerical models. When provision for these scales (horizontal, vertical, and temporal) is made, a cloud overlap assumption of some sort appears to be necessary to account for the fact that clouds are likely not to fill a whole grid box, particularly when the effect of the radiation transfer is not computed at every time step of the model. In this instance, the radiative forcing, and its impact on the atmosphere, obtained when averaging all-or-nothing clouds is likely to differ from the one obtained considering partial cloudiness, with im-

pact, for example, on the temporal variability of precipitation.

A full study of the response of the ECMWF model to changes in horizontal or vertical resolution is out of the scope of this paper [and can be found for older versions of the model in Boyle (1993); Gleckler and Taylor (1993), Potter (1995), and Phillips et al. (1995)]. However, a related question is whether and how these effects of the COA on model fields actually depend on the model horizontal and vertical resolutions. All results presented in the previous sections have been obtained
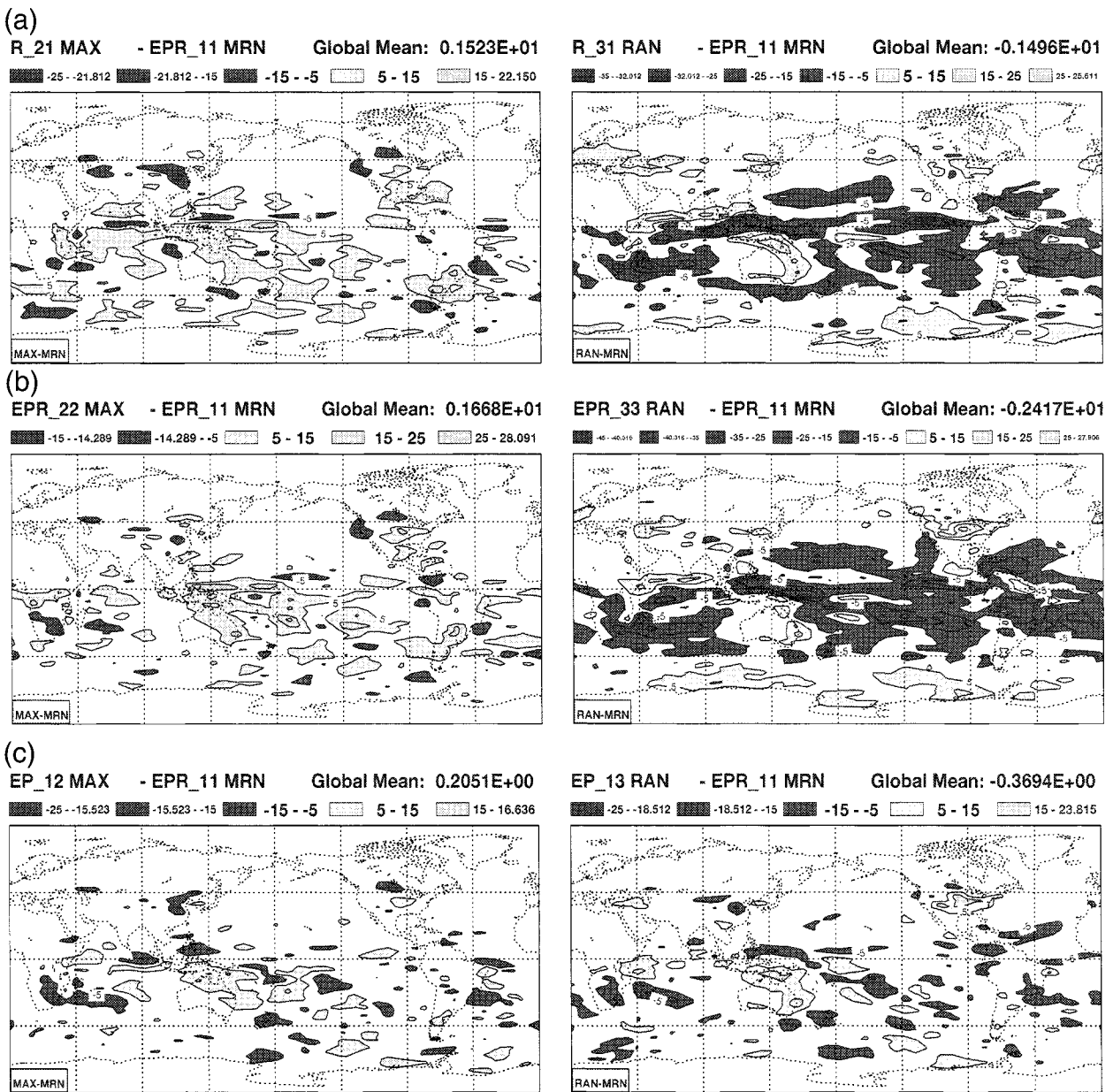
FIG. 13. Differences in absorbed SW radiation at TOA (W m^{-2}), between MAX–MRN (left panels) and RAN–MRN (right panels) for the RAD (top), EPR (middle), and EP (bottom) simulations. Step is 10 W m^{-2} starting from ± 5 W m^{-2}.

with the ECMWF model with 31 levels between the surface and 10 hPa, and a horizontal resolution corresponding to a (1.875°)^2 grid in the Tropics. To study the dependence of the COA results on model vertical resolution, we have repeated the EPR experiments with the ECMWF model, run either with 19 levels between the surface and 10 hPa (hereafter T$_L$95 L19), or with a new (experimental) 60-level version discretization, which includes 46 layers over the same slice of the atmosphere (the 14 extra layers are located in the stratosphere up to 0.2 hPa). Unfortunately, this 60-level ver-

sion was not available for the model with the linear grid: Results are therefore for a T63 horizontal resolution [corresponding to the same (1.875°)^2 grid than T$_L$95 and for a four-month simulation starting on 30 October 1986 (hereafter T63 L60)]. To study the dependence of the COA results on horizontal resolution, simulations were also repeated with the 31-level model with a T42 [grid is (2.8125°)^2], T$_L$159 [grid is (1.125°)^2], and T$_L$319 [grid is (0.5625°)^2] horizontal resolution (hereafter T42 L31, T$_L$159 L31, and T$_L$319 L31). Table 7 presents both the globally averaged total cloud cover
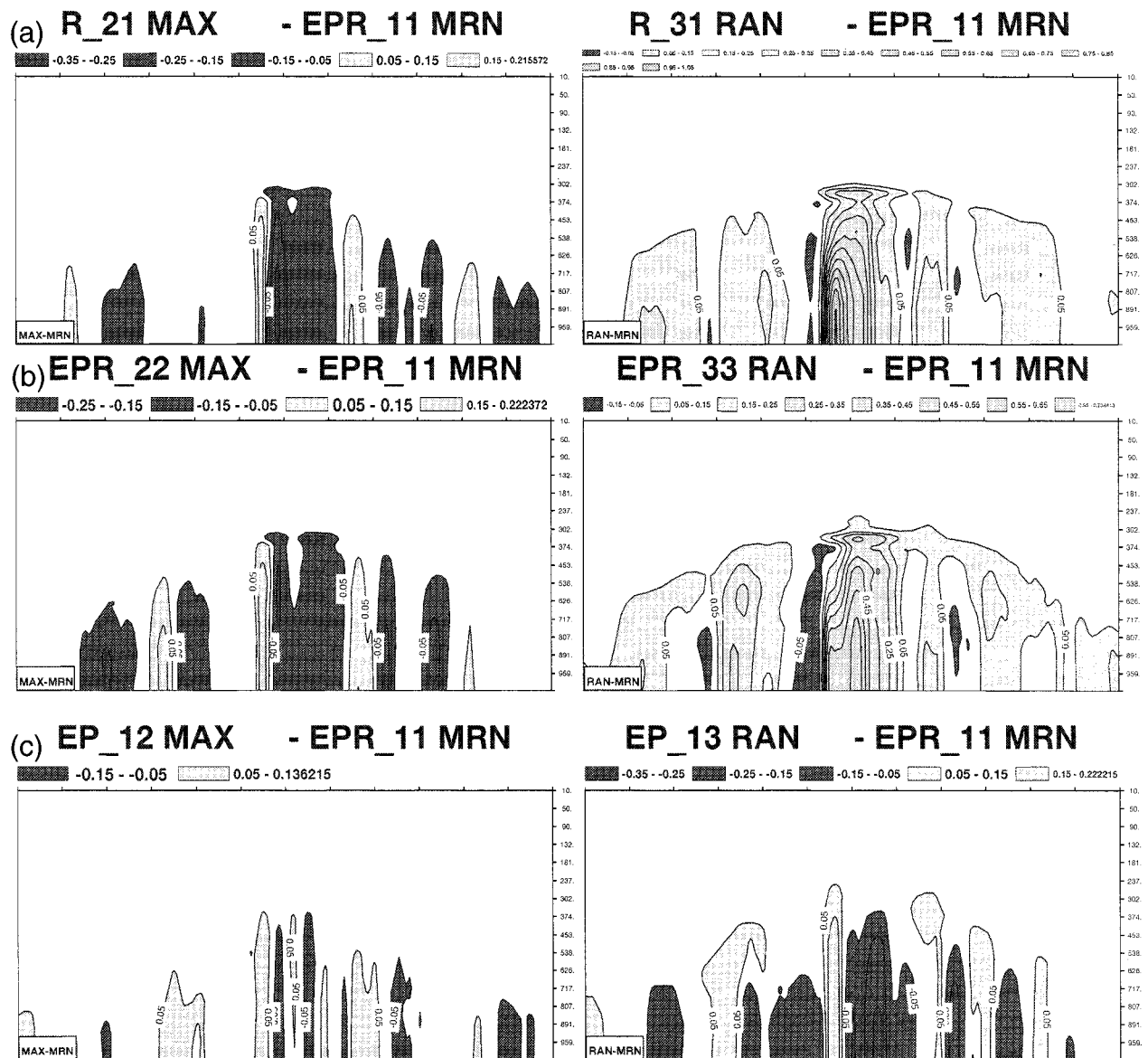
FIG. 14. Differences in zonally averaged flux of total precipitation (kg m^{-2} day^{-1}), between MAX–MRN (left panels) and RAN–MRN (right panels) for the RAD (top), EPR (middle), and EP (bottom) simulations. Solid precipitation occurs above the thick line, liquid precipitation below it. Step is 0.06 kg m^{-2} day^{-1} starting from ±0.03 kg m^{-2} day^{-1}.

and the MRN-equivalent cloud cover for the various model configurations, whereas Table 8 gives the corresponding globally averaged radiative fluxes at the top of the atmosphere. Figure 20 compares the MAX–MRN and RAN–MRN differences in total cloud cover for these various model configurations. Whatever the model configuration is, the model behavior with respect to a change in COA has the same characteristics: the RAN–MRN (respectively MAX–MRN) changes in total cloudiness are generally positive (respectively negative) over most of the latitude range. As expected, the effects of the COA on model fields depend much more on the vertical than on the horizontal resolution. The L19 re-

sults display a smaller amplitude than the L31 and L60 ones, reflecting the more limited choice in the potential cloud vertical distributions. Interestingly, the experimental L60 model shows a sensitivity to COA similar to that of the L31 model, although the total cloud cover is larger due to a larger amount of both almost transparent high clouds and more developed subtropical stratocumulus clouds off the western facades of the continents (not shown). In terms of dependence on the model horizontal resolution, the T42 L31 RAN–MRN changes in TCC are smaller in amplitude than those obtained with the T_L95 L31, T_L159 L31, and T_L319 L31 models. These latter three sets of results are roughly

(a)

R_21 MAX   - EPR_11 MRN   Global Mean: -0.103E-01

R_31 RAN   - EPR_11 MRN   Global Mean: 0.275E-01

(b)

EPR_22 MAX   - EPR_11 MRN   Global Mean: -0.246E-02

EPR_33 RAN   - EPR_11 MRN   Global Mean: 0.262E-01

(c)

EP_12 MAX   - EPR_11 MRN   Global Mean: 0.580E-02

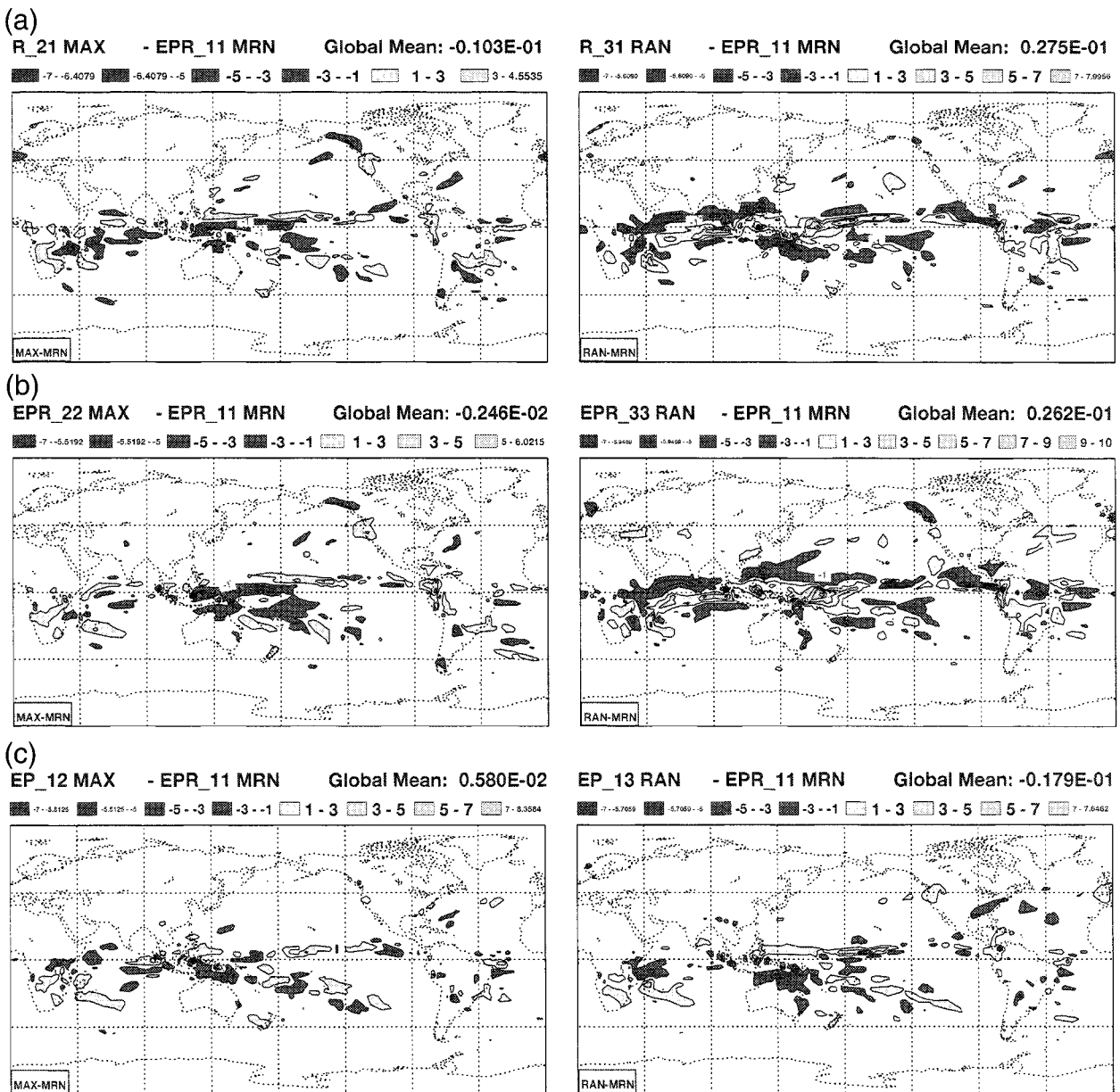**EP_13 RAN   - EPR_11 MRN   Global Mean: -0.179E-01**

FIG. 15. Differences in total precipitation (mm day^{-1}), between MAX–MRN (left panels) and RAN–MRN (right panels) for the RAD (top), EPR (middle), and EP (bottom) simulations. Step is 2 mm day^{-1} from ± 1 mm day^{-1}.

similar, indicating a convergence with increasing horizontal resolution of the model cloud distribution (at least when seen in terms of zonally averaged quantities).

When changing the cloud overlap assumption in a model, the most dramatic effect is seen in the radiation fields, as the horizontal (and to a smaller extent the vertical) redistribution of the cloud layers strongly affects the vertical radiative profiles. This makes the RAD and EPR simulations similar in most respects, in particular for all parameters in direct relation with the three-dimensional distribution of radiation: radiative fields at TOA, and surface, vertical distributions of LW and SW

heating rates, and temperature. In our experiments based on the ECMWF T$_L$95 L31 model, the MAX and MRN results are relatively close to each other, showing that for this already relatively high vertical resolution and with clouds that can form in any model layers, the majority of clouds tend to form in contiguous layers. The RAN configuration, which forces a vertical decoupling of cloud layers steming from a given physical process (usually the large-scale ascent, or convection) differs largely from the other two configurations. Compared to MRN, the smaller total cloud cover in MAX allows more cooling to space, thus giving a slightly colder and
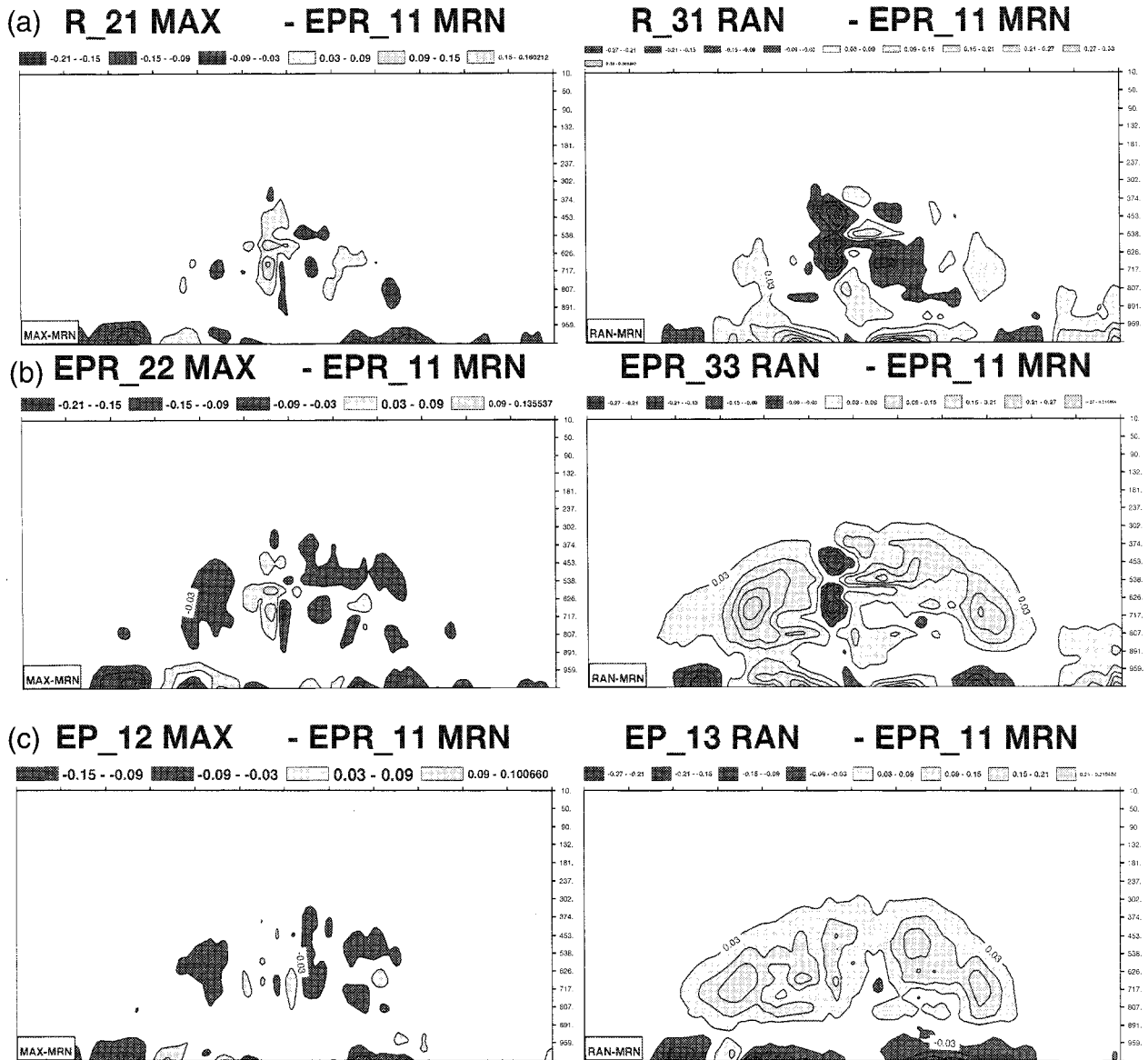
FIG. 16. Differences in zonally averaged evaporation of snow/rain (kg m^{-2} day^{-1}), between MAX–MRN (left panels) and RAN–MRN (right panels) for the RAD (top), EPR (middle), and EP (bottom) simulations. Snow evaporation occurs mainly above the thick line, rain evaporation below it. Step is 0.06 kg m^{-2} day^{-1} starting from ±0.03 kg m^{-2} day^{-1}.

drier atmosphere. On the contrary, RAN results show a higher total cloud cover and increased greenhouse effect particularly in the Tropics, with increased temperature and consequently higher specific humidity below the upper layers of clouds.

When the cloud overlap assumption is also used consistently within the precipitation/evaporation processes of the ECMWF prognostic cloud scheme, this further strengthens the response of the model to a change in cloud overlap assumption. However, as the evaporation of precipitation from the clouds is a relatively small term in the moisture budget of the atmosphere, the impact of a consistent treatment of the cloud overlap for the precipitation/evaporation processes is much smaller than its impact on radiation, the direct effect of a consistent COA for precipitation/evaporation being outweighed by the opposing indirect effect on radiation.

Due to the lack of available observations on cloud overlap, this study is based only on model simulations. A recent study by Barker et al. (1999) addresses the impact of various assumptions for the vertical structure of clouds, on the resulting shortwave fluxes and heating rates, from Monte Carlo simulations performed on the fields produced by a large-eddy simulation model, for which a 0 or 1 cloud occurrence is justified. Similar studies including longwave radiation transfer and pre-
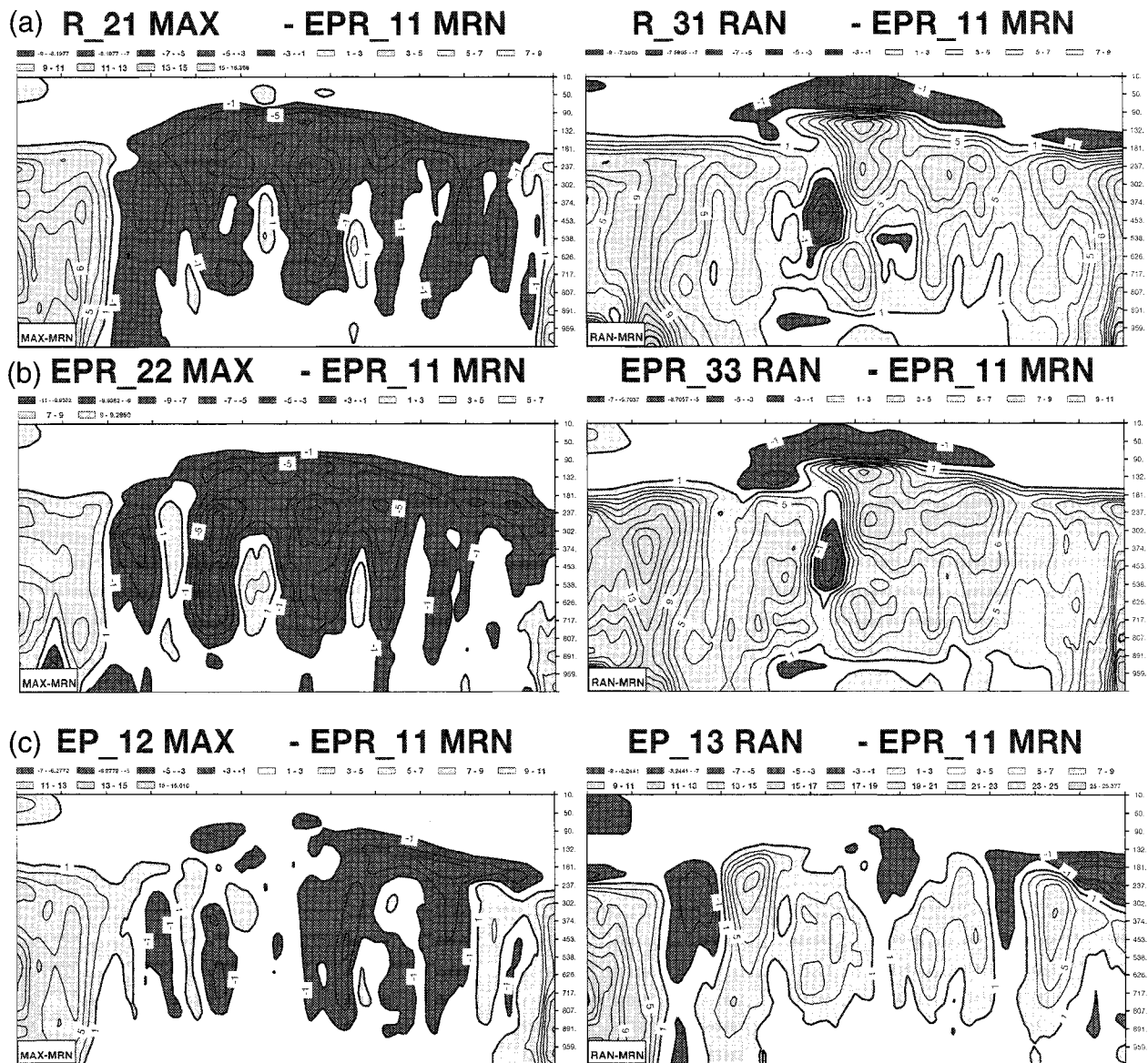
FIG. 17. Zonally averaged vertical distributions of the normalized difference in specific humidity, between MAX–MRN (left panels) and RAN–MRN (right panels) for the RAD (top), EPR (middle), and EP (bottom) simulations. Step is 2 percent starting from ±1%.

cipitation/evaporation processes might be a step forward toward designing consistent GCM-type parametrizations.

There is no simple answer to what the minimum vertical resolution of a model should be. The ECMWF atmospheric model is part of the Integrated Forecasting System (developed in cooperation with Météo-France) and is used for medium-range forecasting, data assimilation, probabilistic forecasting, wave forecasting coupled to a wave model, and seasonal forecasting coupled to an ocean model. Its use for assimilating operational meteorological data requires a relatively high vertical resolution to make good use of the satellite radiance information. As a forecast model, it also requires a prop-

er definition of the planetary boundary layer and of the high troposphere–tropopause–lower stratosphere transition region. As of April 1999, the ECMWF model is run every day at T_L319 L50 for the operational reference forecast, and at T_L159 L31 to create the ensemble of 50 simulations used for Monte Carlo forecasting. Every day, a 200-day simulation with the T_L95 L31 atmosphere–ocean coupled model is also run and serves to build an ensemble then used for seasonal (four to six month) forecasts. Over this variety of horizontal (and vertical) resolutions, the maximum-random cloud overlap assumption appears to be the most adequate. However, this adequacy is not established from observations of cloud overlap, but from the agreement between model
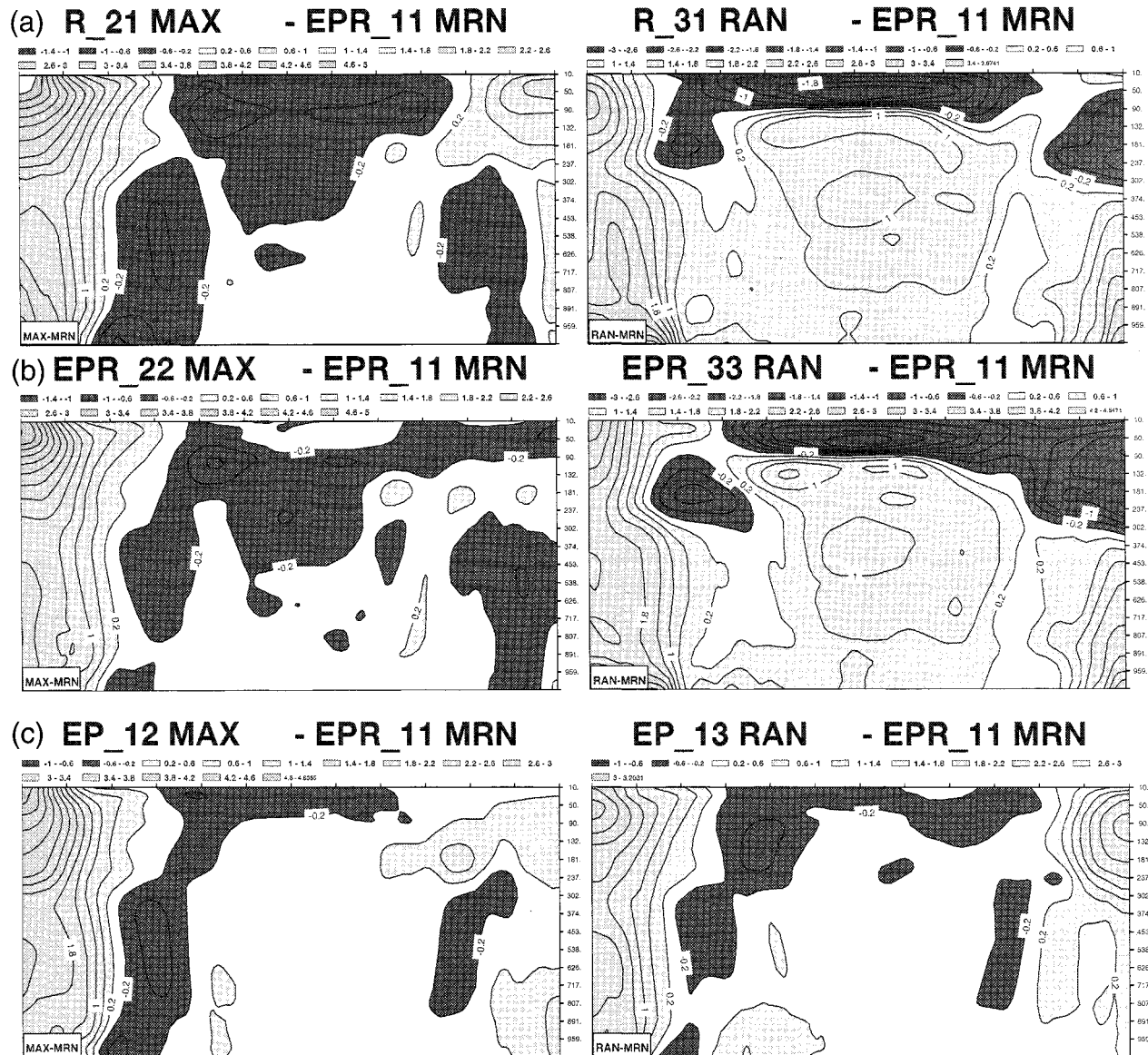
FIG. 18. Differences in zonally averaged vertical distributions of temperature (K), between MAX–MRN (left panels) and RAN–MRN (right panels) for the RAD (top), EPR (middle), and EP (bottom) simulations. Step is 0.4 K starting from ±0.2 K.

and observations, in terms of the parameters that can be verified. This includes comparisons not only with cloud parameters derived from ISCCP, and TOA radiative fluxes and cloud radiative effects derived from ERBE (in offline simulations), but also verification of the model total cloud cover, 2-m temperature, and dewpoint temperature against measurements from the operational synoptic network, to which is added some verification of the surface radiation against some Baseline Surface Radiation Network, Atmospheric Radiation Measurement Program, and Surface Radiation Budget Network station measurements.

From the observational point of view, the coming generation of satellite-embarked together with the ground-based lidar and radar should provide more information on the vertical distribution of cloudiness. However, in the near future, the available and proposed measurements will mainly include data from nonscanning instruments (the Lidar In-space Technology Experiment and TMI, etc.). The measured quantities will essentially be subgrid scale to the current climate and NWP model grids. How these measurements should be aggregated both horizontally and vertically for meaningful comparisons with models is a challenge for the years to come and might be helped by studies such as Barker et al. (1999).

Given the large sensitivity of both the model total cloud cover and the radiation fields to the COA used

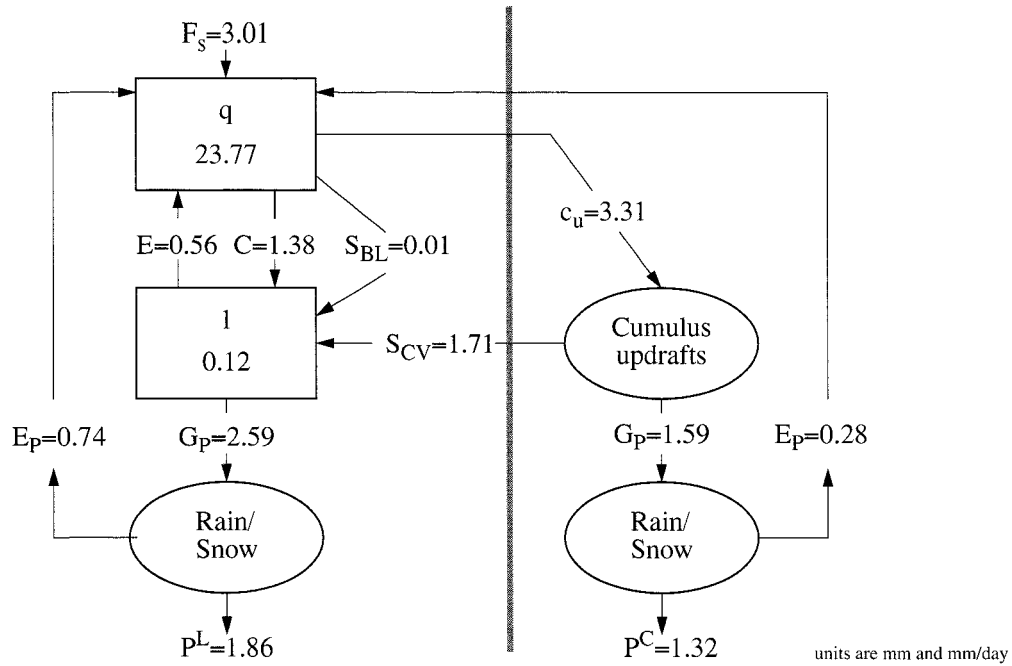Global Mean Hydrological Cycle - D87JF88 - T_L95L31 - EPR/MRN

FIG. 19. The components of the moisture budget of the atmosphere for the EPR–MRN simulation. The left part of the figure corresponds to the effects of the large-scale cloud processes, whereas the right part deals with those from the convective processes. Here q and l are, respectively, the atmospheric water vapor and the cloud ice/water content (both in mm); F_S is the source of water vapor due to the turbulent surface fluxes (in mm day^{-1}). All the remaining terms are conversion terms (also in mm day^{-1}): C is the rate of condensation/sublimation, E that of evaporation of cloud water/ice, G_P is the rate of generation of precipitation by conversion of cloud droplets into raindrops and deposition of cloud ice, E_P the rate of evaporation of precipitation, C_U represents the condensation in the convective updrafts, and S_{CV} and S_{BL} are the sources of cloud water/ice from convection and boundary layer turbulence.

in the radiation scheme, it is very important that these quantities not be validated independently from each other, and of the COA itself. The impact of the COA on the precipitation/evaporation processes within the ECMWF prognostic cloud scheme is of second-order importance. However, as consistency between these and the radiative processes can be obtained with very little impact on the efficiency of the model calculations, it is recommended that it should be included.

APPENDIX A

Implementation of the Various COAs in the Radiation Scheme

In the longwave part of the spectrum, the ECMWF radiation scheme is a so-called emissivity scheme. It does not account for clear-sky longwave scattering and clouds are simply taken as black- or graybodies. In this

TABLE 5. The components of the surface energy budget. SLHF is the surface latent heat flux, and SSHF is the surface sensible heat flux. All fluxes in W m^{-2}.

	Evaporation–precipitation–radiation			Radiation		Evaporation–precipitation	
	MRN	MAX	RAN	MAX	RAN	MAX	RAN
STR	−57.7	−59.6	−50.4	−59.4	−50.9	−57.8	−57.5
SSR	166.1	168.0	164.3	167.7	165.5	166.4	165.6
SLHF	−87.8	−87.8	−87.9	−87.5	−88.0	−87.9	−87.3
SSHF	−12.7	−12.8	−12.6	−12.7	−12.6	−12.8	−12.9

TABLE 6. The components of the moisture budget of the atmosphere for the various sets of simulations. Units are mm and mm day^{-1}.

Variable	Evaporation–precipitation–radiation			Radiation		Evaporation–precipitation	
	MRN	MAX	RAN	MAX	RAN	MAX	RAN
F_s	3.008	3.028	3.045	3.007	3.057	3.007	3.002
q	23.77	23.57	24.56	23.81	24.49	23.68	24.06
E	0.560	0.558	0.592	0.558	0.568	0.554	0.583
C	1.380	1.366	1.685	1.380	1.636	1.378	1.434
S_{BL}	0.013	0.014	0.015	0.014	0.015	0.014	0.013
I	0.125	0.123	0.136	0.129	0.125	0.120	0.122
S_{CV}	1.714	1.713	1.731	1.708	1.694	1.701	1.749
E_P	0.740	0.731	0.854	0.749	0.764	0.733	0.844
G_P	2.595	2.581	2.889	2.591	2.829	2.587	2.659
P_L	1.855	1.850	2.035	1.842	2.065	1.854	1.815
c_u	3.306	3.340	3.194	3.319	3.122	3.296	3.393
$E_P{}^c$	0.276	0.286	0.271	0.282	0.254	0.280	0.299
$G_P{}^c$	1.592	1.627	1.463	1.611	1.428	1.595	1.644
P_C	1.316	1.341	1.192	1.329	1.174	1.315	1.345

case, the use of a different cloud overlap assumption simply translates into a different rule (see section 2a) to compute the ''obscuration matrix,'' which, from a given atmospheric level, defines how much each of the other layers contribute to the flux at this level (see Fig. 1). Each layer contributes from its clear-sky fraction and cloudy fraction (if any). The ''obscuration matrix'' defines the cloud cover CC_{IJ} encountered between level I where the flux is required and any other level J in the atmosphere.

The multiple scattering in the shortwave part of the spectrum makes the problem more difficult to solve exactly. We have considered an exact solution only for the directly transmitted flux (the parallel beam) and an approximate treatment for the diffuse radiation. The original formulation of the shortwave radiation scheme (Fouquart and Bonnel 1980) simply includes a linear weighting of the respective clear and cloudy reflectivities and transmissivities according to their fractions in the layer, and Morcrette and Fouquart (1986, hereafter MF86) showed that this approach produces results in very close agreement with the full random overlap assumption.

TABLE 7. Total cloud cover and MRN-diagnostic cloud cover for a series of four-month simulations at different model horizontal and vertical resolutions. All results are global means averaged over the last three months (DJF). TCC is the total cloud cover, whereas MRN is a diagnostic total cloud cover computed assuming a maximum-random overlapping of cloud layers (see Table 3 and text, section 4a).

	TCC			MRN		
	MRN	MAX	RAN	MRN	MAX	RAN
T42 L31	0.653	0.633	0.689	0.641	0.638	0.635
T_L95 L31	0.657	0.626	0.718	0.642	0.638	0.638
T_L159 L31	0.659	0.633	0.713	0.636	0.630	0.640
T_L319 L31	0.647	0.631	0.703	0.637	0.643	0.639
T_L95 L19	0.643	0.624	0.680	0.630	0.631	0.626
T63 L60	0.728	0.686	0.797	0.707	0.698	0.702

To deal with the different COAs, we modified the formulation discussed in MF86 and introduced an alternate formulation that consists of the following.

1) Defining the clear-sky and cloudy fractions of the atmospheric column accounting for the relevant COA. These are defined as the corresponding fractions as seen from the surface after integrating from the top down.
2) Computing an effective cosine of the solar zenith angle μ_e relative to only the cloudy part of the atmospheric column:

$$\mu_e = \left\{\frac{[1 - C_{\text{eff}}(j)]}{\mu_0} + rC_{\text{eff}}(j)\right\}^{-1},$$

where $C_{\text{eff}}(j)$ is the total cloudiness over level j, computed from the top of the atmosphere with the relevant COA; r is the diffusivity factor; and μ_0 is the cosine of the solar zenith angle.
3) Using the clear-sky solar zenith angle μ_0 in the clear-sky fraction of the column, only slightly modified when going from the top to the bottom of the atmosphere to account for Rayleigh scattering in clear air.
4) Computing the reflectivity Re_{clr} and transmissivity Tr_{clr} for the fraction of the layer in the clear-sky column as function of $\mu_0(j)$, and Re_{cdy} and Tr_{cdy} for the fraction of the layer in the cloudy column as a function of $\mu_e(j)$.
5) Combining the Re and Tr separately for the cloudy and clear-sky fractions of the column to get the relevant upward and downward fluxes (as done in MF86).
6) Combining the clear-sky and cloudy fluxes before going out of the SW radiation scheme to get the fluxes for the grid box.
   • The effective zenith angle μ_e keeps the same expression (6a) of MF86 but the amount of cloudiness CC encountered by the parallel beam on its way between the TOA and the top of a considered

TABLE 8. The components of the radiation budget at the top of the atmosphere for one four-month simulation at different model horizontal and vertical resolutions. Results are presented averaged over the last three months. OLR is the outgoing longwave radiation; ASW is the shortwave absorbed radiation. Units are W m^{-2}.

	OLR			ASW		
	MRN	MAX	RAN	MRN	MAX	RAN
T42 L31	−240.5	−242.5	−234.2	250.4	251.4	249.4
T$_L$95 L31	−241.9	−243.8	−234.5	248.5	250.3	246.5
T$_L$159 L31	−243.1	−244.6	−235.5	248.0	250.2	245.7
T$_L$319 L31	−243.3	−244.5	−236.4	248.9	250.1	246.6
T$_L$95 L19	−236.6	−237.0	−230.8	254.7	254.9	253.4
T63 L60	−240.6	−242.9	−231.0	244.8	246.6	242.2

layer depends on the chosen COA and can take any of the expressions in section 2a. Within the framework of MF86, this ensures the correct solution for the parallel beam in the clear-sky fraction at the surface, and the correct solution for the illumination of the top of any cloudy layer by the parallel beam.

- The clear-sky and cloudy reflectivities and transmissivities, Re$_{clr}$, Re$_{cdy}$, Tr$_{clr}$, Tr$_{cdy}$ [Eqs. (4) and (5) of MF86], are modified to account for the fact that the reflectivity R_u of the underlying layer either comes from the cloudy or the clear-sky fraction of this layer. This is equivalent to enforcing the correct solution for a given COA but only with respect to a given layer and the one immediately underneath. All other layers below contribute as in the original formulation of the scheme, namely under the random overlap assumption.

As seen in Tables 1 and 2 and Fig. 2, this approximate treatment produces only small systematic differences in both the fluxes at the boundaries and in terms of absorption of shortwave radiation within the clouds. Fur-

thermore this approximate solution allows the different COAs to be implemented in the ECMWF radiation scheme, with only a small increase in computational time (<1% of the time required for the SW computations).

APPENDIX B

Implementation of the Various COAs in the Cloud Scheme

Within the prognostic cloud scheme, in any layer from the uppermost cloud layer downward, both a precipitation flux and an evaporation rate may be computed. Precipitation produced in the cloudy fraction falls and contributes either to collection of cloud water by raindrops within an underlying cloud layer or to evaporation within the same layer but in the clear-sky fraction located under the precipitating cloud.

In all three sets of simulations discussed here (RAD, EPR, and EP), the cloud overlap assumptions discussed in section 2 are implemented in the prognostic cloud scheme to compute the relevant fractional areas where
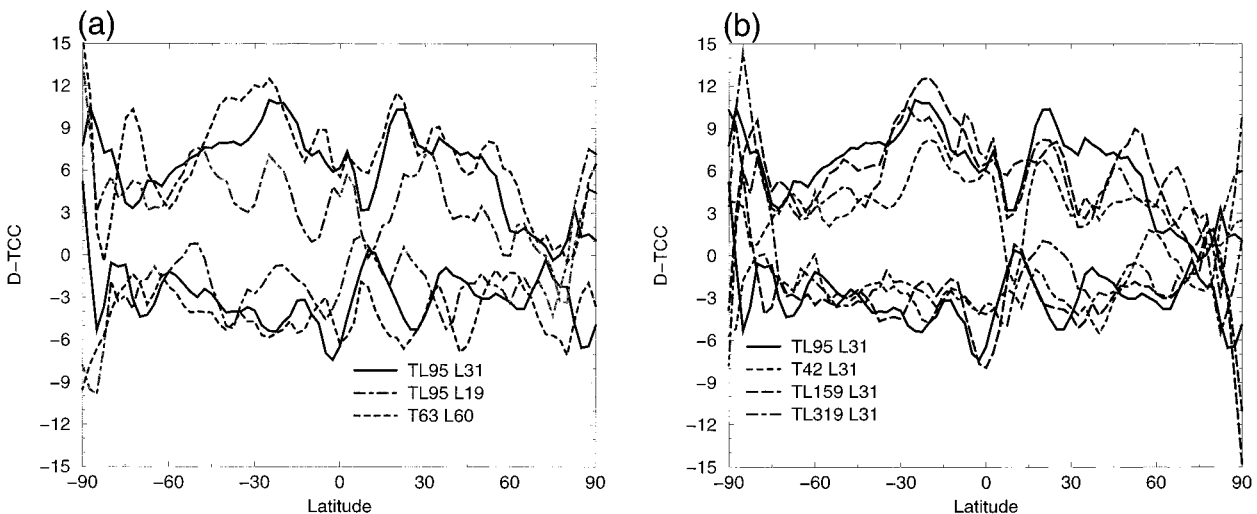

FIG. 20. Changes in total cloud cover (in %) for various vertical (top) and horizontal (bottom) resolutions. Upper curves are for RAN–MRN results, lower curves for MAX–MRN results.

precipitation and evaporation can take place. Four fractional areas are defined, from CC_{0k}, CC_{0k-1}, C_k, and C_{k-1}, which are, respectively, the total cloud cover from the top of the atmosphere to the bottom of layer k, a similar quantity to the bottom of layer $k - 1$, the cloud cover in layer k, and the one in layer $k - 1$. The first area is the clear-sky fraction of the column, where no precipitation or evaporation of cloud water is taking place, corresponding to what is located to the right of the clouds in Fig. 1, that is,

$$A_k^{\text{clear}} = 1 - CC_{0k},$$

where CC_{0k} is defined as in section 2.

The second area is the cloud under clear fraction, corresponding to the total cloud extent for the uppermost cloud, or for subsequent cloud layers, to what is lost to cloud from previously clear fraction,

$$A_k^{0C} = CC_{0k} - CC_{0k-1}.$$

The third area corresponds to the fraction where clouds are adjacent in two consecutive layers, where snow precipitation due to sedimentation of ice and rain precipitation due to collection of cloud water by raindrops might occur. For MRN and MAX, it is calculated as

$$A_k^{\text{CC}} = \min(C_k, C_{k-1}),$$

whereas for RAN, it is calculated as

$$A_k^{\text{CC}} = \max(0, CC_{0k-1} - CC_{0k} + C_k).$$

Finally the fourth area is the clear-sky fraction of the layer overlaid by higher-level cloudiness where evaporation of precipitation coming from above might take place. It is calculated as

$$A_k^{C0} = CC_{0k} - A_k^{\text{CC}} - A_k^{0C}.$$

REFERENCES

Barker, H. W., G. L. Stephens, and Q. Fu, 1999: The sensitivity of domain-averaged solar fluxes to assumptions about cloud geometry. *Quart. J. Roy. Meteor. Soc.,* **125,** 2127–2152.

Boyle, J. S., 1993: Sensitivity of dynamical quantities to horizontal resolution for a climate simulation using the ECMWF (cycle 33) model. *J. Climate,* **6,** 816–838.

Brankovic, C., T. N. Palmer, and L. Ferranti, 1994: Predictability of seasonal atmospheric variations. *J. Climate,* **7,** 217–237.

Charlock, T., F. Rose, T. Alberta, G. L. Smith, D. Rutan, N. Manalo-Smith, P. Minnis, and B. Wielicki, 1994: Cloud profiling radar requirements: Perspectives from retrievals of the surface and atmospheric radiation budget and studies of atmospheric energetics. Rep. of GEWEX Topical Workshop on Utility and Feasibility of a Cloud Profiling Radar, WCRP-84, IGPO Publication Ser. No. 10, B10–21.

Cubasch, U., 1981: Comparison of the influence of different radiation parameterizations on 10-day forecasts. *Proc. ECMWF Workshop on Radiation and Cloud–Radiation Interaction in Numerical Modelling,* Reading, United Kingdom, ECMWF, 55–73.

Ebert, E. E., and J. A. Curry, 1992: A parameterization for ice optical properties for climate models. *J. Geophys. Res.,* **97** (D), 3831–3836.

Fouquart, Y., 1987: Radiative transfer in climate models. *Physically-Based Modelling and Simulation of Climate and Climatic Chang-*

es, M. E. Schlesinger, Ed., NATO ASI Series, Kluwer Academic, 223–284.

——, and B. Bonnel, 1980: Computations of solar heating of the earth's atmosphere: A new parameterization. *Beitr. Phys. Atmos.,* **53,** 35–62.

Geleyn, J.-F., and A. Hollingsworth, 1979: An economical analytical method for the computation of the interaction between scattering and line absorption of radiation. *Beitr. Phys. Atmos.,* **52,** 1–16.

——, A. Hense, and H.-J. Preuss, 1982: A comparison of model generated radiation fields with satellite measurements. *Beitr. Phys. Atmos.,* **55,** 253–286.

Glecker, P. J., and K. E. Taylor, 1993: The effect of horizontal resolution on ocean surface heat fluxes in the ECMWF model. *Climate Dyn.,* **9,** 17–32.

Gregory, D., J.-J. Morcrette, Ch. Jakob, and A. Beljaars, 1998: Introduction of revised radiation, convection, cloud and vertical diffusion schemes into Cy18r3 of the ECMWF integrated forecasting system. ECMWF Tech. Memo. 254, 39 pp.

Heymsfield, A. J., and L. J. Donner, 1990: A scheme for parameterizing ice–cloud water content in general circulation models. *J. Atmos. Sci.,* **47,** 1865–1877.

Hortal, M., 1998: T_L319 resolution and revised orographies. ECMWF Research Department Mem. R60.5/MH/23, 18 pp.

——, and A. J. Simmons, 1991: Use of reduced Gaussian grids in spectral models. *Mon. Wea. Rev.,* **119,** 1057–1074.

Jakob, Ch., 1994: The impact of the new cloud scheme on ECMWF's Integrated Forecasting System. *Proc. Workshop on Modelling, Validation and Assimilation of Clouds,* Reading, United Kingdom, ECMWF, 277–294.

——, and S. A. Klein, 1999a: The role of vertically varying cloud fraction in the parametrization of microphysical processes in the ECMWF model. *Quart. J. Roy. Meteor. Soc.,* **125,** 941–965.

——, and ——, 1999b: A parametrization of the effects of cloud and precipitation overlap for use in general circulation models. *Quart. J. Roy. Meteor. Soc.,* in press.

Liang, X.-Z., and W.-C. Wang, 1997: Cloud overlap effects on GCM climate simulations. *J. Geophys. Res.,* **102** (D), 11 039–11 047.

Matveev, L. T., 1984: *Cloud Dynamics.* D. Reidel, 340 pp.

McClatchey, R. A., R. W. Fenn, J. E. A. Selby, F. E. Volz, and J. S. Garing, 1972: Optical properties of the atmosphere. AFCRL 72-0479, Environ. Res. Paper 411, Bedford, MA, 108 pp.

Morcrette, J.-J., 1990: Impact of changes to the radiation transfer parameterizations plus cloud optical properties in the ECMWF model. *Mon. Wea. Rev.,* **118,** 847–873.

——, 1991: Radiation and cloud radiative properties in the ECMWF forecasting system. *J. Geophys. Res.,* **96** (D), 9121–9132.

——, and J.-F. Geleyn, 1985: On the influence of different radiation parameterizations on model-generated radiation fields. *Quart. J. Roy. Meteor. Soc.,* **111,** 565–585.

——, and Y. Fouquart, 1986: The overlapping of cloud layers in shortwave radiation parameterizations. *J. Atmos. Sci.,* **43,** 321–328.

Nordeng, T. E., 1994: Extended versions of the convection parametrization scheme at ECMWF and their impacts upon the mean climate and transient activity of the model in the tropics. ECMWF Tech. Memo. 206, 25 pp.

Phillips, T. J., L. C. Corsetti, and S. L. Grotch, 1995: The impact of horizontal resolution on moist processes in the ECMWF model. *Climate Dyn.,* **11,** 85–102.

Potter, G. L., 1995: The effect of horizontal resolution on cloud radiative forcing in the ECMWF model. PCMDI Rep. 22, University of California, Livermore, CA, 28 pp.

Smith, E. A., and L. Shi, 1992: Surface forcing of the infrared cooling profile over the Tibetan Plateau. Part I: Influence of the relative longwave radiative heating at high altitude. *J. Atmos. Sci.,* **49,** 805–822.

Stubenrauch, C. J., A. D. Del Genio, and W. B. Rossow, 1997: Implementation of subgrid cloud vertical structure inside a GCM and its effect on the radiation budget. *J. Climate,* **10,** 273–287.

Tian, L., and J. Curry, 1989: Cloud overlap statistics. *J. Geophys. Res.,* **94** (D), 9925–9936.

Tiedtke, M., 1989: A comprehensive massflux scheme for cumulus parameterization in large scale models. *Mon. Wea. Rev.,* **117,** 1779–1800.

——, 1993: Representation of clouds in large-scale models. *Mon. Wea. Rev.,* **121,** 3040–3061.

Wang, J., and W. B. Rossow, 1995: Determination of cloud vertical structure from upper-air observations. *J. Appl. Meteor.,* **34,** 2243–2258.

——, and ——, 1998: Effects of vertical structure on atmospheric circulation in the GISS GCM. *J. Climate,* **11,** 3010–3029.